

Multicarrier Interactions in Semiconductor Nanocrystals in Relation to the Phenomena of Auger Recombination and Carrier Multiplication

Victor I. Klimov

Chemistry Division, C-PCS, Los Alamos National Laboratory, Los Alamos, New Mexico 87545; email: klimov@lanl.gov

Annu. Rev. Condens. Matter Phys. 2014. 5:285–316

First published online as a Review in Advance on January 10, 2014

The *Annual Review of Condensed Matter Physics* is online at conmatphys.annualreviews.org

This article's doi:
10.1146/annurev-conmatphys-031113-133900

Copyright © 2014 by Annual Reviews.
All rights reserved

Abstract

Chemically synthesized semiconductor nanocrystals (NCs) have been extensively studied as a test bed for exploring the physics of strong quantum confinement and as a highly flexible materials platform for the realization of a new generation of solution-processed optical, electronic, and optoelectronic devices. Because of readily tunable, size-dependent emission and absorption spectra, colloidal NCs are especially attractive for applications in light-emitting diodes, solid-state lighting, lasing, and solar cells. It is universally recognized that the realization of these and other prospective applications of NCs requires a detailed understanding of carrier-carrier interactions in these structures, as they have a strong effect on both recombination and photogeneration dynamics of charge carriers. For example, non-radiative Auger recombination is one of the key factors limiting the performance of NC-based lasers and light-emitting diodes. The inverse of this process, carrier multiplication, plays a beneficial role in light harvesting and can be used to boost the efficiency of photovoltaics through increased photocurrent. This article reviews recent progress in the understanding of multicarrier processes in NCs of various complexities, including zero-dimensional spherical quantum dots, quasi-one-dimensional nanorods, and various types of core-shell heterostructures. This review's specific focus is on recent efforts toward controlling multicarrier interactions using traditional approaches, such as size and shape control, as well as newly developed methods involving interface engineering for suppression of Auger decay and engineering of intraband cooling rates for enhancement of carrier multiplication.

1. INTRODUCTION

Semiconductors are widely used as both light emitters and light harvesters in a range of applications, including light-emitting diodes (LEDs), lasers, photodetectors, and photovoltaic (PV) cells. Two characteristics of any material that are of key importance to these applications are the emission wavelength (defines the color of generated light) and the spectral onset of optical absorption (defines how much of the solar spectrum can be converted to electrical charges). Both of these parameters are controlled by the width of the energy gap (E_g) separating the conduction and the valence band (**Figure 1a**). In semiconductors of macroscopic sizes (i.e., bulk semiconductors), the width of this gap for a given material is a fixed parameter. However, the situation changes in the case of nanoscale semiconductor particles or nanocrystals (NCs) with sizes smaller than ~ 10 nm (**Figure 1b**). This size range corresponds to the regime of quantum confinement for which electronic excitations feel the presence of the particle boundaries and respond to changes in the particle size by adjusting their energy spectra. This phenomenon is known as the quantum size effect, and nanoscale particles that exhibit it are often referred to as quantum dots (QDs). In the present review, the term quantum dot is used in reference to spherically (or near spherically) shaped zero-dimensional nanostructures, whereas the more general term nanocrystal is used in relation to a crystalline nanostructure of an arbitrary shape.

As was just pointed out, a key feature of NCs is a size-dependent band-gap energy. Specifically, as the NC size decreases, the energy gap increases, leading to a blue shift of both the emission wavelength and the spectral onset of optical absorption. In the first approximation, this effect can be described using a simple quantum-box model (1, 2). For a spherical QD with radius R , this model predicts that a size-dependent contribution to the energy gap is simply proportional to $1/R^2$:

$$E_g(\text{QD}) = E_{g0} + \frac{\hbar^2 \pi^2}{2m_{eh} R^2},$$

where E_{g0} is the bulk semiconductor band-gap energy, $m_{eh} = m_e m_h / (m_e + m_h)$, and m_e and m_h are the electron and hole effective masses respectively. In addition to increasing the energy gap, quantum confinement leads to a transformation of the continuous energy bands of a bulk material into discrete, atomic-like energy levels. These well-separated QD states can be labeled using atomic-like notations (1S, 1P, 1D, etc.), as illustrated in **Figure 1b**. This discrete structure of energy states leads to correspondingly discrete features in the absorption spectrum of QDs (schematically shown by colored bars in **Figure 1c**), in contrast to the continuous absorption spectrum of a bulk semiconductor (black line in **Figure 1c**).

Using colloidal chemical syntheses, semiconductor NCs can be prepared with nearly single atomic layer precision and have sizes from a few to tens of nanometers and size dispersions as narrow as 4%–5% (3). In addition to nearly spherical QDs, modern chemical methods allow for fabrication of NCs of other shapes, including nanorods of controlled aspect ratios (4), pyramidal particles (5), nanoplatelets (6), and tetrapods (7). Further, additional flexibility in controlling NC properties is provided by heterostructuring when two or more different materials are combined within the same nanoparticle. Examples of hetero-NCs include all-semiconductor core-shell structures (8–10) and bicomponent nanorods and tetrapods (11–13) as well as various types of semiconductor-metal hybrids (14–16). The combination of tunable electronic and optical spectra and chemical flexibility make colloidal QDs ideally suited for bottom-up assembly into optical device structures, including LEDs (17–19), lasers (20, 21), photodetectors (22, 23), and PVs (24–26).

An important property of semiconductor NCs is a significant enhancement in carrier-carrier Coulomb interactions, which leads to a number of novel physical phenomena, including large

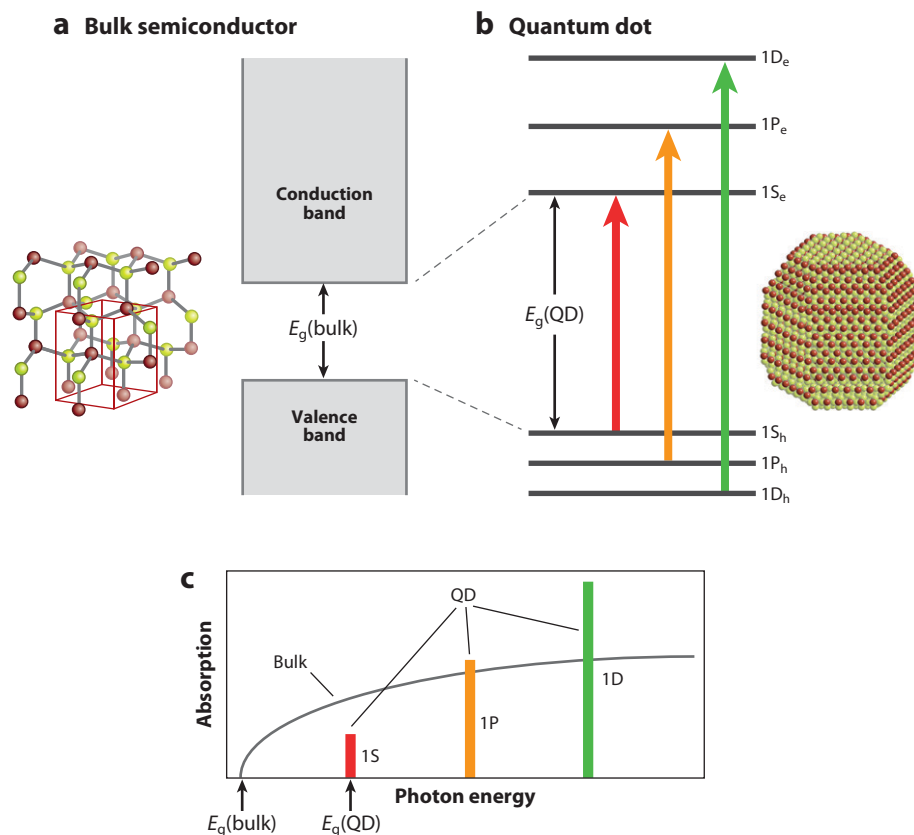


Figure 1

(a) A bulk semiconductor has continuous conduction and valence energy bands separated by a fixed energy gap, E_g . (b) A quantum dot (QD), however, is characterized by discrete atomic-like states with energies that are determined by the QD radius R . These well-separated QD states can be labeled using atomic-like notations ($1S_e$, $1P_e$, $1D_e$, etc. for electrons and $1S_h$, $1P_h$, $1D_h$, etc. for holes). (c) A schematic representation of a continuous absorption spectrum of a bulk semiconductor (gray line) compared with a discrete absorption spectrum of a QD (colored bars).

splitting of electronic states induced by electron-hole (e-h) exchange coupling (27), high-efficiency intraband relaxation due to e-h energy transfer (28, 29), ultrafast multiexciton decay by Auger recombination (30, 31), and high-efficiency generation of multiple e-h pairs (multiexcitons) by single photons via carrier multiplication (CM) (32–34). Significant interest in multiexciton phenomena in NCs has been stimulated by studies of NC lasing (20, 35, 36) as well as by the significant potential of CM in PVs (37, 38). Realization of both of these applications requires detailed understanding of dynamical and spectral properties of multiexcitons in NCs.

The focus of this article is on two multicarrier phenomena: Auger recombination and CM. Auger recombination is a process in which the e-h recombination energy is not emitted as a photon but is transferred to a third carrier, promoting it to a higher-energy state either within a NC or outside it (Auger ionization). In bulk semiconductors, Auger recombination is inhibited by kinematic restrictions that are imposed by energy and translational-momentum conservation (39). However, because of relaxation of momentum conservation, Auger recombination rates increase

dramatically in zero-dimensional NCs (40, 41). CM can be considered as the inverse of Auger recombination. In this process, a hot carrier relaxes by transferring its energy to a valence band electron, which is promoted to the conduction band. Although it is inefficient in bulk semiconductors, especially in the range of photon energies relevant to solar energy conversion, this process is enhanced in quantum confined NCs (32–34, 42), making it a viable mechanism for boosting the efficiency of PV devices.

This review discusses several new aspects of Auger recombination and CM with a focus on recent efforts for controlling these processes via advanced heterostructuring and/or engineering of NC interfaces. Specific topics overviewed here include the scaling of Auger decay rates with NC occupancy for both neutral and charged excitations, the role of interfacial alloying (as it specifically affects the shape of the interfacial potential) in Auger recombination, and practical approaches for suppression of Auger decay in heterostructured QDs by introducing an intermediate alloy layer at the core-shell interface. Then, we discuss the connection between Auger decay and CM in the context of a window-of-opportunity model, in which Auger recombination lifetimes are used as a surrogate for time constants of an individual CM event. We also overview experimental studies that demonstrate a significant effect of non-CM intraband energy losses on the overall CM performance and describe the most recent efforts on cooling-rate engineering, using dual-emitting PbSe/CdSe QDs with an especially thick shell that allow for a manifold enhancement of CM yields compared to core-only PbSe QDs.

2. AUGER DECAY OF NEUTRAL AND CHARGED MULTICARRIER STATES

2.1. Scaling of Auger Lifetimes with Quantum Dot Occupancy

An important mechanism for nonradiative losses in QDs is associated with Auger recombination of multicarrier states, i.e., states involving more than just one electron and one hole. The simplest of these states are charged excitons, or negative (Figure 2a) and positive (Figure 2b) trions (X^- and X^+ , respectively). In addition to radiative or extrinsic defect-related processes, charged excitons can decay via nonradiative Auger recombination, which is extremely efficient in QDs and is characterized by time constants that can be much shorter than time scales of intrinsic radiative decay.

Although photoexcitation can also produce charged species (via so-called photoionization), it usually results in neutral excitations, such as single e-h pairs (excitons), double e-h pairs (biexcitons), or other higher-multiplicity states. The simplest neutral multiexciton state is a biexciton (Figure 2c). As in the case of trions, normally its decay in QDs is dominated by Auger recombination. In fact, the biexciton Auger decay rate (k_{2A}) can be related to those of the negative and positive trions (k_{-1A} and k_{+1A} , respectively) by $k_{2A} = 2(k_{-1A} + k_{+1A})$. In core-only QDs that feature mirror-symmetric conduction and valence bands, $k_{-1A} = k_{+1A} = k_{2A}/4$. Such a situation is realized, for example, in PbSe QDs for which the observed trion Auger lifetimes ($\tau_{-1A} = 1/k_{-1A}$ and $\tau_{+1A} = 1/k_{+1A}$) are indeed approximately four times longer than that of a biexciton ($\tau_{2A} = 1/k_{2A}$) (43).

In order to describe recombination of higher-order excitations that contain N e-h pairs (N -exciton state with $N > 2$), one can apply statistical arguments (44), i.e., assume that the probability of an Auger recombination event is proportional to the product of the number of all possible conduction-band to valence-band transitions (expressed as N^2 ; Figure 2d) and the number of carriers that can accept the energy released in a given interband transition [expressed as $(2N - 2)$]. The scaling of multiexciton lifetimes in this statistical case is given by $k_{NA} = \tau_{NA}^{-1} \propto N^2(N - 1)$ or

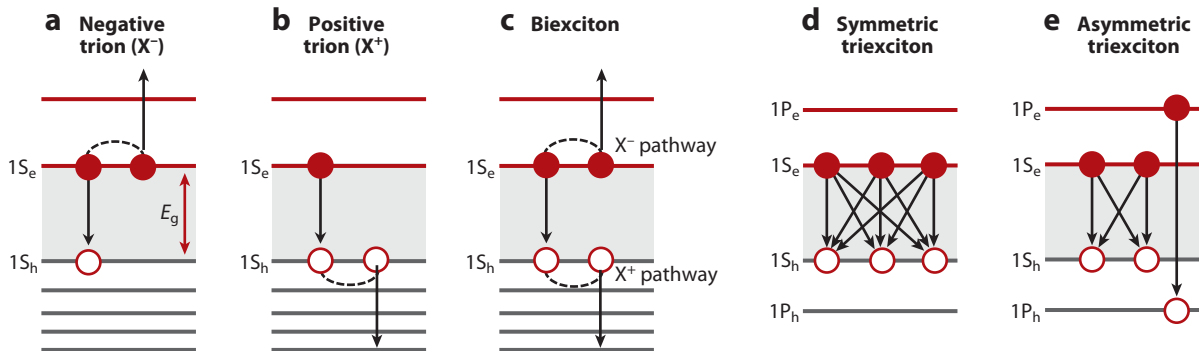


Figure 2

(a) Nonradiative Auger recombination of a negative trion can be described in terms of Coulomb scattering between the two conduction-band electrons when one of them undergoes an interband transition (electron-hole recombination) while the other is excited within the conduction band. (b) A similar description applies to Auger recombination of a positive trion, which can be described in terms of Coulomb scattering between the two valence-band holes. (c) Auger recombination of a biexciton can involve re-excitation of either an electron (negative trion pathway) or a hole (positive trion pathway). Given that the biexciton comprises two electrons and two holes, its Auger decay rate is twice the sum of the X^- and X^+ Auger decay rates: $k_{2A} = 2(k_{-1A} + k_{+1A})$. (d) Possible conduction-band to valence-band transitions in the case of Auger recombination of a symmetric 1S1S1S triexciton. (e) Possible conduction-band to valence-band transitions in the case of Auger recombination of an asymmetric 1S1S1P triexciton, assuming that the S-P interband transitions are much weaker than the S-S and P-P transitions.

$$\tau_{NA} = 4\tau_{2A}[N^2(N-1)]^{-1}, \quad 1.$$

if expressed in terms of the biexciton lifetime (τ_{2A}); k_{NA} and τ_{NA} are, respectively, the rate and the time constant of Auger decay of the N -exciton state.

We can further generalize Equation 1 for the situation of charged multicarrier states when the electron occupancy of the QD (N_e) is not necessarily equal to its hole occupancy (N_h). In this case, the number of possible e-h transitions is given by the product $N_e N_h$, whereas the total number of energy transfer pathways is $(N_e + N_h - 2)$. The Auger decay rate of the $(N_e; N_h)$ state is proportional to the product of these two values, which yields the following expression for the Auger lifetime:

$$\tau_{N_e, N_h A} = 8\tau_{2A}[N_e N_h (N_e + N_h - 2)]^{-1}. \quad 2.$$

In standard monocomponent NCs, Auger recombination lifetimes are orders of magnitude shorter than radiative time constants (τ_r) (31, 45), which leads to very low quantum yields (QYs) of multiexciton emission. Further, because radiative rates scale more slowly with NC occupancy than do Auger decay rates, the QY decreases with increasing order of the multicarrier state. To quantify the dependence of QY on QD occupancy, we apply statistical arguments to the emission rate of the $(N_e; N_h)$ state ($r_{N_e, N_h} = 1/\tau_{N_e, N_h r}$), which yields $r_{N_e, N_h} = r_1(N_e N_h)$, where $r_1 = r_{1,1}$ is the single-exciton radiative rate. Assuming that $\tau_{N_e, N_h A} \ll \tau_{N_e, N_h r}$ (which is valid in all standard core-only or thin-shell NCs) and further neglecting all non-Auger related carrier losses, we can present the photoluminescence (PL) QY as

$$QY_{N_e, N_h} = (8\tau_{2A}\tau_{1r}^{-1})/(N_e + N_h - 2). \quad 3.$$

This expression is valid only if at least one of the occupation numbers (N_e or N_h) is greater than unity. For neutral multiexcitons ($N_e = N_h = N > 1$), $QY_N = (4\tau_{2A}\tau_{1r}^{-1})/(N-1)$.

Strictly speaking, the above consideration of statistical scaling of multicarrier radiative and nonradiative decay rates can only be applied in a situation in which all carriers occupy electronic

states of identical symmetries. Such an ideal situation is most nearly realized, once again, in QDs of PbSe, in which the electron and the hole band-edge 1S levels are eightfold degenerate (a combined result of twofold spin degeneracy and the existence of four equivalent minima located at the L points of the Brillouin zone) (46, 47) and hence, one can expect to observe statistical scaling of τ_N up to $N = 8$. Indeed, experimental studies of PL dynamics (48) indicate that the ratios of the biexciton-to-exciton (r_2/r_1) and triexciton-to-exciton (r_3/r_1) radiative rates measured for PbSe QDs are close to 4 and 9, respectively, as expected from statistical arguments.

The analysis of radiative lifetimes in NCs with a lower degree of degeneracy of band-edge states also suggests an approximate validity of statistical scaling for, at least, biexciton states. For example, studies of CdSe QDs with a twofold-degenerate band-edge 1S_e level indicate the r_2/r_1 ratio of ~ 3.5 (49). This value is in agreement with the results of more recent ensemble measurements that indicate r_2/r_1 of 3–5 (50). Recent single-dot studies of CdSe/CdS core-shell structures with a range of shell thicknesses show that the pump-power dependence of PL intensity can be closely reproduced using statistical arguments (51).

The scaling of Auger lifetimes for neutral excitations has often been inferred from the ratio of the biexciton and triexciton time constants (31, 44). According to statistical scaling, this ratio should be 4.5. Measurements of CdSe QDs, however, usually indicate a smaller ratio. In an early attempt to experimentally determine the scaling of Auger lifetimes in CdSe QDs (31), multiexciton dynamics were studied by monitoring carrier-induced bleaching of the band-edge 1S absorption feature with a femtosecond transient absorption (TA) experiment, in which the QD sample excited with a short sub-picosecond pulse at ~ 3 eV was probed with variably delayed weak pulses of a femtosecond white-light continuum. According to these measurements the τ_{2A}/τ_{3A} ratio varied from ~ 2.3 for dots with $R = 1.45$ nm to ~ 3.4 for $R = 4.2$ nm. These results were confirmed by recent ultrafast cathodoluminescence studies of a series of thin-shell CdSe/ZnS QDs that produced τ_{2A}/τ_{3A} ratios ranging from ~ 2.3 to ~ 3.3 (52). The observed deviation from ideal statistical scaling ($\tau_{2A}/\tau_{3A} = 4.5$) in the case of CdSe QDs can be rationalized if one accounts for the fact that the 1S state can accommodate only two electrons; hence, the triexciton, in addition to S-type carriers, also contains carriers in states of other symmetries (asymmetric triexciton). For example, if we assume that both the electron and the hole of the third exciton occupy the first-excited 1P state (the 1S1P triexciton; **Figure 2e**) and further neglect the S-P interband transitions, we find that τ_{2A}/τ_{3A} is 2.5. This value is significantly smaller than that for purely statistical scaling and is closer to quadratic scaling ($\tau_{NA} \propto N^2$) when $\tau_{2A}/\tau_{3A} = 2.25$, which was described in Reference 44 as “quantum mechanical” and was used to explain early observations in Reference 31.

The τ_{2A}/τ_{3A} ratios measured for PbSe NCs are usually larger than those for CdSe NCs and indicate that the τ_N scaling is at least cubic ($\tau_{NA} \propto N^3$). In order to distinguish between cubic and statistical scalings, the TA dynamics measured across a wide range of pump intensities were analyzed using a set of coupled-rate equations (44). For larger QDs ($R = 4$ nm), this analysis indicated that the measured time transients could be best described by statistical scaling. The distinction between cubic and statistical scalings was more subtle in smaller, 2-nm QDs, as both types of scalings explained experimental data reasonably well.

2.2. Auger Recombination of Charged States in Chemically Doped Quantum Dots

Recently, several experimental works have addressed the problem of lifetime scaling for QD charged states. In some of these measurements, extra charges have been generated via either photoionization during optical excitation (48, 53) or impact ionization in the case of excitation with a short pulse of energetic electrons (52). Better control over the degree of charging has been achieved by introducing the extra carriers into QDs either electrochemically (54, 55) or using chemical reductants (43).

In one example of this latter type of study (43), extra electrons were injected into the quantum-confined states of PbSe and PbS QDs using treatment with molecules of cobaltocene, which is a mild reducing agent. Its reduction potential [-0.69 V versus the standard hydrogen electrode (SHE) (56)] is above the conduction-band edge of both bulk PbSe (0.2 V versus SHE) and PbS (0.1 V versus SHE) (57), suggesting the possibility of ground-state electron transfer from cobaltocene to these semiconductors. However, for QDs of these materials, the conditions for electron transfer change as a result of the effects of quantum confinement. Specifically, as the electron $1S_e$ band-edge level shifts up in energy with decreasing QD size (Figure 3a), the driving force for charge transfer decreases up to the point at which the process becomes unfavorable. On the basis of size-dependent $1S_e$ energies (58), one can expect that cobaltocene-to-QD electron transfer shuts off for particle diameters smaller than ~ 3.2 nm (PbSe QDs) and ~ 4.2 nm (PbS QDs) (Figure 3a).

Following electron transfer to the $1S_e$ state, the QD band-edge ($1S$) absorption peak is expected to be bleached (Figure 3b) due to state filling (Pauli blocking). In the case of PbSe and PbS QDs, with an eightfold degenerate $1S_e$ state (46), the bleach amount ($\Delta\alpha_{1S}$) scales linearly with the number of extra electrons (N_e): $|\Delta\alpha_{1S}|/\alpha_{0,1S} = |\alpha_{1S} - \alpha_{0,1S}|/\alpha_{0,1S} = N_e/8$ (59), where $\alpha_{0,1S}$ and α_{1S} are the amplitudes of the $1S$ absorption peak in the untreated and treated samples, respectively. Indeed, when cobaltocene is mixed with PbSe QDs, the $1S$ peak amplitude is reduced (Figure 3c), which is similar to the effect observed in previous studies on electrochemical charge injection (60). In the experiments in Reference 43, the effect was most pronounced in the biggest QDs (7.9 -nm diameter; $E_g = 0.60$ eV), for which the driving force for electron transfer is the largest. In these dots, the $1S$ feature was completely bleached, indicating the injection of at least eight electrons per QD in the ensemble. The band-edge bleach decreased in smaller QDs until it became virtually unnoticeable in the smallest particles (Figure 3c, solid and dashed purple lines), for which the driving force is the lowest (Figure 3a).

In addition to modifying interband absorption involving valence-band to conduction-band transitions, doping is expected to give rise to a new midinfrared absorption feature due to activation of an intraband transition, which promotes the injected electrons from the $1S_e$ to the $1P_e$ level (60, 61) (Figure 3b). As the second peak in interband absorption is due to the $1S_h$ – $1P_e$ and $1P_h$ – $1S_e$ transitions (they have nearly identical energies) (62) (Figure 3d), its separation from the $1S$ peak provides a measure of the energy of the intraband $1S_e$ to $1P_e$ transition, which for 7.9 -nm PbSe QDs is 165 meV (43) (Figure 3d, black solid line). Indeed, along with $1S$ bleaching, cobaltocene treatment of the QDs produced a new midinfrared feature located exactly at 165 meV (Figure 3d, red dashed line), confirming that the charges were indeed introduced into the quantized $1S_e$ level.

The studies found in Reference 43 indicate that doping has a dramatic effect on PL efficiency (Figure 4a) and on the dynamics of photogenerated carriers in PbSe QDs (Figure 4b) that are primarily due to activation of an additional recombination channel associated with fast non-radiative Auger decay. On the basis of statistical considerations (see Section 2.1) the radiative lifetime of an exciton in the presence of N_e extra charges, $\tau_{(N_e+1),1r}$, is shorter than that of a neutral exciton [typically hundreds of nanoseconds (63)] by a factor of $(N_e + 1)$. In reality, due to activation of Auger recombination, if even one additional electron is introduced into the QD, the measured lifetime of the singly charged exciton (τ_{-1A}) is reduced down to subnanosecond timescales (53). Therefore, PL QY of a charged sample is dominated by the QDs that remain neutral (i.e., uncharged). Assuming that the distribution of extra charges across an ensemble is Poissonian, the fraction of uncharged dots can be found from $f_0 = \exp(-\langle N_e \rangle)$, where $\langle N_e \rangle$ is the average per-dot doping level in the sample. By plotting f_0 as a function of $\langle N_e \rangle$ derived from the bleach of the $1S$ absorption peak, one can indeed closely describe the experimental results on PL quenching without any adjustable parameters (solid line in inset of Figure 4a; data shown by symbols are from Reference 43).

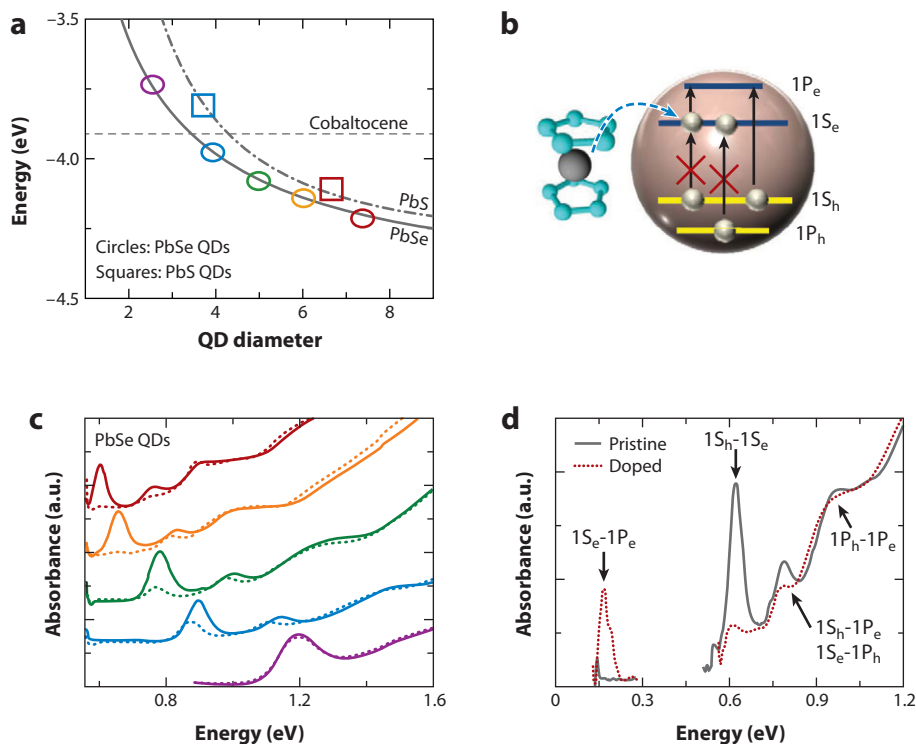


Figure 3

(a) An energy level diagram illustrating the redox potential of cobaltocene (dashed black line) in comparison to the conduction-band states in PbSe (solid gray line) and PbS (dash-dot gray line) quantum dots (QDs). Colored symbols correspond to PbSe (circles) and PbS (squares) QD samples studied in Reference 43. (b) Illustration of the effect of electron injection from cobaltocene on optical absorption of a QD. The interband $1S_h-1S_e$ and $1P_h-1S_e$ features are bleached because of blocking (partial or complete) of the $1S_e$ state by the injected electrons. This is accompanied by the development of a new mid-infrared absorption feature caused by the intraband $1S_e-1P_e$ transition. (c) The QD size-dependent absorption spectra of PbSe QDs before (solid lines) and after (dashed lines) treatment with cobaltocene; color coding matches that in panel a. Note that the effect of the bleaching of the band-edge absorption feature associated with electron injection increases with decreasing E_g , i.e., increasing QD size. (d) Mid- to near-infrared absorption spectra of pristine (solid gray line) and cobaltocene-treated (dashed red line) PbSe QDs with a band gap of ~ 0.6 eV. The treated sample exhibits a new mid-infrared band at 165 meV, which matches the energy spacing between the $1S_e$ and the $1P_e$ electronic states, as expected for the intraband $1S_e-1P_e$ transition. Adapted from Reference 43.

A TA experiment was utilized to directly monitor the effect of doping on carrier dynamics (43). **Figure 4b** shows a series of TA dynamics measured at the center of the $1S$ transition as a function of doping level (PbSe QDs with $E_g = 0.67$ eV). Initially, the sample was doped with approximately four electrons per dot, as inferred from the magnitude of the $1S$ bleach. The sample chosen for these measurements did not have any protective CdSe coating and was gradually losing extra charges on the timescale of a few hours, which was accompanied by recovery of the $1S$ absorption feature. [This behavior is in contrast to PbSe/CdSe core-shell QDs that maintained doping for at least a month (43)]. The TA traces were taken at different times during this recovery and were analyzed using a double exponential fit in order to capture the exciton lifetimes in the most heavily and most lightly doped NCs. The results are plotted in **Figure 4c** and compared with the Auger lifetimes of an exciton with 1, 2, 3, and 4 extra charges ($X_{-1} = X^-$, X_{-2} , X_{-3} and X_{-4} , respectively),

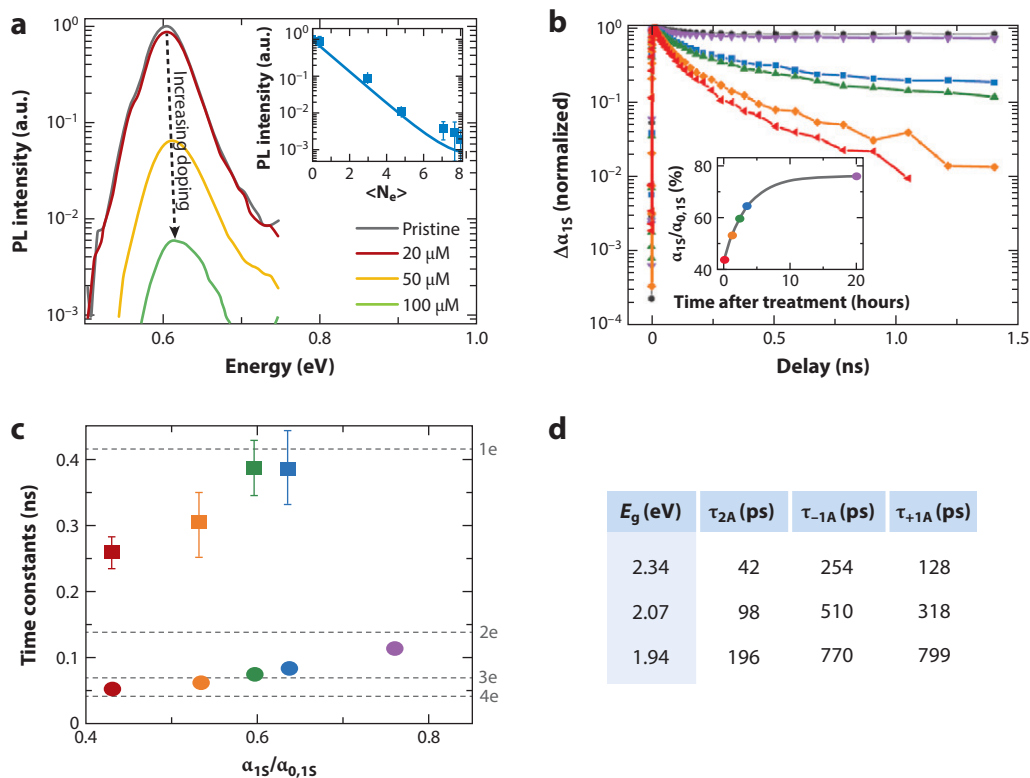


Figure 4

(a) Cobaltocene concentration-dependent photoluminescence (PL) quenching of PbSe quantum dots (QDs). Inset: PL intensity (symbols) as a function of the average number of injected electrons derived from $\langle N_e \rangle = 8|\Delta\alpha_{1s}/\alpha_{0,1s}|$, along with the calculated PL intensity (line). (b) 1S bleach dynamics of the cobaltocene-treated PbSe QD sample during 1S absorption recovery (inset) measured using excitation at 1.55 eV with a pump flux of ~ 0.4 photons absorbed per pulse per QD. Color coding is the same in the main panel and in the inset; different colors correspond to different times after treatment with cobaltocene (see inset). (c) Two time constants (symbols; color coding is the same as in panel b) of the recovering sample derived from a double exponential fit of the measured 1S bleach decay. Horizontal dashed lines represent Auger lifetimes of an exciton in the presence of different numbers of excess electrons from 1 to 4. (d) Auger recombination lifetimes of biexcitons (τ_{2A}), and negative (τ_{-1A}) and positive (τ_{+1A}) trions in standard thin-shell CdSe/ZnS QDs with different band gaps. Adapted from References 43 and 52.

which were calculated using statistical scaling from the biexciton lifetime ($\tau_{2A} = 104$ ps; measured for the pristine undoped sample). For example, based on the latter value, the lifetime of the singly charged exciton (negative trion) is $\tau_{-1A} = 4\tau_{2A} = 416$ ps.

The comparison indicates that the shortest time constant measured for the freshly treated sample is close to that of $X_{-} - -_1$, as expected for NCs doped with ~ 4 electrons, whereas the long time constant lies in between the values estimated for X_{-1} and $X_{-,-1}$. During the 1S bleach recovery, the initial time constant becomes progressively longer as a result of discharging of the NCs and eventually approaches the value expected for a negative trion.

The fact that in PbSe QDs τ_{-1A} is approximately four times the biexciton lifetime suggests that $\tau_{-1A} = \tau_{+1A}$, as expected for a material with mirror symmetric conduction and valence bands. The symmetry between the X_{-} and X_{+} recombination pathways can be distorted in QDs of II–VI semiconductors because of a significant difference between the conduction and valence bands. Specifically, a much higher density of valence-band states favors the positive trion Auger

recombination channel (**Figure 2b**), for which the energy conservation requirement is easier to meet. Recent measurements (52) have evaluated the biexciton and negative trion Auger lifetimes in thin-shell CdSe/ZnS QDs using picosecond time-resolved cathodoluminescence. The results of these measurements are summarized in **Figure 4d** (τ_{+1A} is derived from the measured τ_{-1A} and τ_{2A}). One can see that in larger dots ($E_g = 1.94$ eV), τ_{+1A} and τ_{-1A} are close to each other (770 ps and 799 ps, respectively). However, as the dot size is decreased, the X^- Auger pathway gets progressively suppressed because of increasing separation between the conduction-band states so that in QDs with $E_g = 2.34$ eV, the Auger lifetime of the positive trion (129 ps) is approximately half as long as that of the negative trion (254 ps).

The asymmetry between the X^- and X^+ recombination pathways is further enhanced in core-shell structures that feature a significant difference in effective localization radii of electrons (R_e) and holes (R_h). For example, in so-called giant quasi-type-II CdSe/CdS core-shell QDs (g-QDs) (64, 65), which feature very thick shells, the electron is delocalized over the entire nanostructure, whereas the hole is confined to the smaller core; hence, R_e is much greater than R_h . This enhances the Auger decay rate of the positive versus negative trion because of increased probability of hole-hole scattering events (involved in the X^+ decay channel; **Figure 2c**) compared with electron-electron scattering (involved in the X^- decay channel; **Figure 2c**). For example, based on a recent experimental study of core-shell CdSe/CdS QDs (66), in samples with core radius $r = 1.5$ nm and shell thickness $H = 5.5$ nm, $\tau_{-1A} = 5$ ns and $\tau_{2A} = 0.35$ ns. These values yield $\tau_{+1A} = 0.81$ ns, which suggests a very significant asymmetry between the X^- and X^+ Auger decay channels, with $\tau_{-1A} \approx 6\tau_{+1A}$.

2.3. The Role of Quantum Dot Interfaces in Auger Recombination

As was pointed out in the introduction, Auger recombination complicates practical realization of many QD applications, including LEDs, PV cells, and especially lasers, as all of these applications either rely directly on emission from multiexcitons (lasers) or are influenced by the effects of charging (LEDs, PVs, and single-photon emitters). Therefore, the development of approaches for suppression of Auger recombination represents an important current challenge in the field of colloidal nanostructures.

As was first reported in Reference 31, in monocomponent QDs, the multiexciton Auger recombination time scales linearly with particle volume (sometimes referred to as a V-scaling), which is a universal trend observed for a large number of compositions (41). Although Auger lifetimes exhibit a quick increase with QD size, they are still short (subnanosecond timescale), even in large QDs with sizes approaching that of a bulk exciton. An alternative approach to reducing Auger decay rates is based on inducing spatial separation of electrons and holes, which reduces wavefunction overlap for the ground-state electron and the hole participating in the recombination event. This strategy was explored, for example, using type-II core-shell QDs (35, 67) and dot-in-rod nanostructures (68).

Reduced e-h overlap is also one of the reasons for Auger decay suppression in CdSe/CdS core-shell g-QDs, wherein electrons are delocalized over the entire structure while holes are tightly confined within the small core (51, 64, 69). However, as was pointed out in Reference 70, the V-scaling and the reduced e-h overlap alone were not able to explain very rapid lengthening of the Auger time constant with increasing shell thickness. This observation suggests that other structural characteristics of the QD, such as the properties of its interfaces, might play an important role in Auger recombination.

Indeed, calculations by Cragg & Efros (71), as well as a follow-up theoretical study by Climente et al. (72), have suggested that in addition to QD size, the shape of the confinement potential has

a significant effect on the Auger decay rate. Specifically, these studies demonstrated that by smoothing the confinement potential (by going, for example, from a sharp step-like potential to a smooth parabolic profile) one can reduce the overlap between the initial and the final state of the carrier excited during Auger recombination and thus achieve orders-of-magnitude reduction in the rate of this process. This effect was invoked to explain suppression of blinking (i.e., PL intermittency) in radially alloyed QDs (73) and was likely responsible for the increased intensity of multiexciton emission from CdTe/CdSe QDs that was observed in studies found in Reference 74.

Recently, the correlation between unintentional interfacial alloying and suppression of Auger recombination in CdSe/CdS QDs with varied shell thicknesses was detected by low-temperature fluorescence line-narrowing studies (70). These measurements revealed that prolonged growth of a thick CdS shell was accompanied by the development of a specific phonon-assisted PL feature corresponding to a sum of longitudinal optical (LO) phonon modes of CdSe and CdS; this feature is a signature of formation of a $\text{CdSe}_x\text{S}_{1-x}$ alloy layer at the core-shell interface. Furthermore, it was observed that the increase in the thickness of this layer directly correlated with lengthening of the Auger decay time constant.

The studies in References 66 and 75 directly addressed the problem of the effect of interfacial alloying on Auger recombination by studying carrier dynamics in core-shell CdSe/CdS QDs with a well-defined $\text{CdSe}_x\text{S}_{1-x}$ alloy layer incorporated between core and shell. These studies were enabled by a novel synthesis (66) that allowed for a much faster growth of a thick CdS shell compared to the more traditional successive ionic layer adsorption and reaction (SILAR) method (64, 65); the application of fast shell growth was essential for avoiding unintentional alloying at the CdSe/CdS interface. Using this method, it was possible to synthesize structures with two distinct interfaces: one with a sharp core-shell boundary (core-shell, or C/S, QDs) and the other with a $\text{CdSe}_x\text{S}_{1-x}$ alloy layer incorporated between the core and the shell (core-alloy-shell, or C/A/S, QDs; see **Figure 5a**). Side-by-side studies of spectroscopic properties of these QDs indicated that the incorporation of the interfacial alloy layer did not have any appreciable effect on single-exciton PL, including its peak wavelength (**Figure 5b**), dynamics (**Figure 5c**), or emission QY (**Figure 5d**). However, the properties of biexciton emission were considerably different between the C/S and C/A/S samples.

Figure 6a compares biexciton PL QYs in the two types of samples evaluated from single-QD measurements of the second-order photon correlation function $g^{(2)}(t)$ (75), which represents the probability of detecting a photon at time t , when one PL photon was already detected at time zero. In the case of pulsed excitation, and if $g^{(2)}$ is measured for spectrally integrated PL, the area ratio of the central ($t = 0$) to side ($t = T$; T is the pulse-to-pulse separation) peak is proportional to the ratio of the biexciton (Q_2) to the single-exciton (Q_1) PL QY: $Q_2/Q_1 = g^{(2)}(0)/g^{(2)}(T)$. The $g^{(2)}$ measurements indicate that for the reference C/S dots, the biexciton PL QY is low ($Q_2/Q_1 < 0.03$) and does not significantly vary with H (gray symbols in **Figure 6a**). This behavior is a direct consequence of fast biexciton Auger recombination, which in these structures occurs primarily via a positive-trion pathway involving re-excitation of a hole (**Figure 2c**). As was discussed in the previous subsection, in thick-shell CdSe/CdS QDs, this channel is faster than the X^- pathway and is not significantly influenced by shell thickness, as changes in H do not appreciably change the effective volume of hole localization.

The alloyed QDs exhibit a distinctly different dependence of Q_2/Q_1 on CdS shell thickness. Even the thinnest shell sample ($L = 1.5$ nm and $H = 0.5$ nm; solid blue circles in **Figure 6b**) shows fairly high values of Q_2/Q_1 that are as much as ~ 0.16 for some of the dots (0.11 on average; red symbols in **Figure 6b**). This suggests significant suppression of intrinsic Auger decay due to a smoothed confinement potential at the core-shell interface (71). Interestingly, a further increase in shell thickness does not appreciably affect the average value of Q_2/Q_1 (red circles in **Figure 6a**; blue triangles, squares, and pentagons show measurements for individual QDs). Even

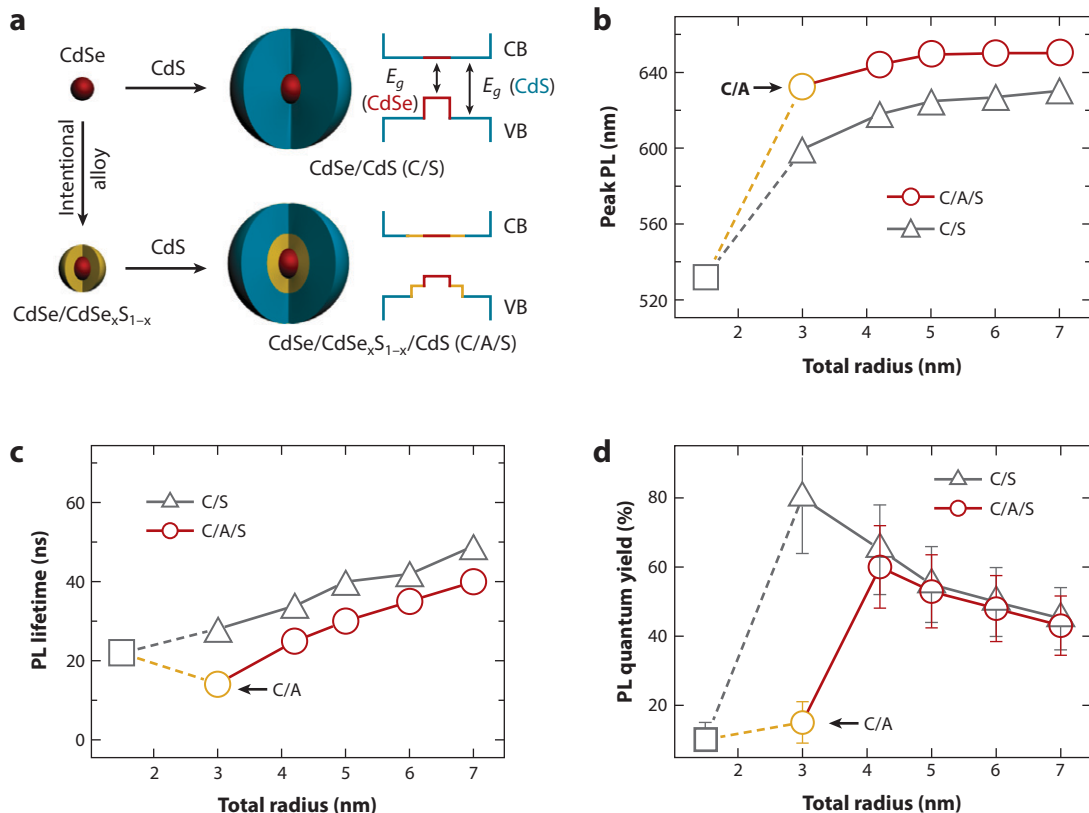


Figure 5

(a) Schematic illustration of the synthesis of core-shell (C/S) and core-alloy-shell (C/A/S) quantum dot (QD) samples with approximate energy diagrams of the resulting structures (CB and VB denote conduction and valence bands, respectively). (b) Photoluminescence (PL) peak wavelengths of C/S (gray symbols) and C/A/S (red symbols) QDs as a function of total QD radius, which varies through varying shell thickness for a fixed core radius of 1.5 nm and a fixed thickness (1.5 nm) of an intermediate alloy layer of CdSe_{0.5}S_{0.5}; the yellow circle shows a C/A sample without an outer CdS shell, and the black square shows a core-only CdSe sample. (c) PL lifetimes for the same samples as in panel b. (d) PL quantum yields for the same samples as in panel b.

for the thickest shell dots ($H = 5$ nm), the average Q_2/Q_1 ratio is only $\sim 40\%$ larger than for dots with $H = 0.5$ nm. This observation implies that the presence of the alloyed layer, rather than the CdS outer shell, plays a principal role in the suppression of biexciton Auger decay (dominated by the X^+ pathway in these QDs) as was suggested by earlier studies of the effect of unintentional alloying (70). Further, these results also suggest that a fairly wide spread in the Q_2/Q_1 values among the dots with a nominally identical total size arises primarily from the variations in the structure of the interfacial alloy layer rather than in the shell thickness or core size.

Recently, practical benefits of interface engineering have been demonstrated via direct studies of the effect of interfacial alloying on the performance of QD-LEDs (Figure 6c) (76). Specifically, a side-by-side comparison of LEDs made of CdSe/CdS QDs with a sharp core-shell interface to LEDs made using similar QDs but with an intermediate CdSe_{0.5}S_{0.5} alloy layer demonstrates that the use of alloyed dots resulted in a sizable improvement of the external quantum efficiency (EQE) as well as a considerable increase of the threshold current for the onset of efficiency roll-off (Figure 6d). Both of these observations can be attributed to the increased emission efficiency of charged

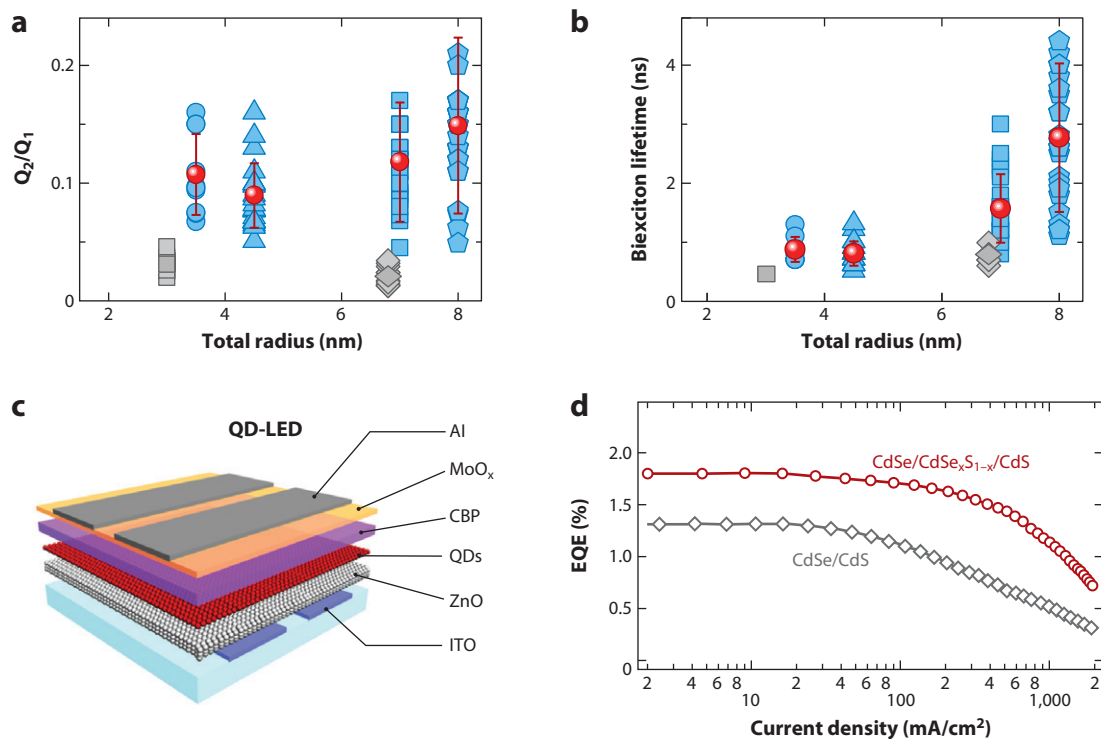


Figure 6

(a) CdS shell-thickness dependence of normalized biexciton photoluminescence (PL) quantum yields (QYs) (Q_2/Q_1) for reference core-shell (C/S; gray) and core-alloy-shell (C/A/S; blue) quantum dots (QDs). The CdS-shell thicknesses for alloyed samples are 0.5 (circles), 1.5 (triangles), 4.0 (squares), and 5.0 nm (pentagons). For the reference QDs, $H = 1.0$ nm (squares) and 5.5 nm (diamonds). For dots with a total radius of 7.0 nm, gray diamonds are slightly shifted left for clarity. Red circles show average values for the alloyed dots. (b) The biexciton lifetime-versus- H dependence for the same samples as in panel a. (c) Schematic illustration of the structure of a QD light-emitting diode (LED) with an inorganic cathode [colloidal particles of zinc oxide (ZnO) deposited on top of an indium tin oxide (ITO) electrode] and a hybrid organic/inorganic anode [a layer of 4,4'-Bis(N-carbazolyl)-1,1'-biphenyl (CBP) separated from an Al electrode by a MoO_x spacer]. Electrons and holes are injected from the ZnO/ITO and the CBP/ MoO_x /Al sides, respectively. (d) External quantum efficiency (EQE) versus current density for two QD-LEDs: one employing CdSe/CdS QDs with an abrupt interface (black diamonds) and the other, CdSe/CdSe $_x$ S $_{1-x}$ /CdS QDs (x is approximately 0.5), with an alloyed interface (red circles). Both QD samples have the same core radius of 1.5 nm and the same total radius of 7 nm; the thickness of the CdSe $_x$ S $_{1-x}$ alloy layer is 1.5 nm. The LED made from alloyed dots shows a higher EQE as well as a higher current for the onset of the EQE roll-off. Adapted from References 75 and 76.

species (including charged excitons and multiexcitons) due to considerable suppression of Auger decay in QDs with alloyed interfaces. These findings demonstrate the large potential of a new approach of interface engineering for manipulating the rate of Auger decay and perhaps of other Auger-type processes, such as Auger ionization (30, 77) and CM (32).

3. CARRIER MULTIPLICATION

3.1. Carrier Multiplication and Solar Energy Conversion

In a traditional photoexcitation scenario, absorption of a photon with energy $\hbar\omega \geq E_g$ results in a single e-h pair, whereas the photon energy in excess of the energy gap is dissipated as heat by exciting lattice vibrations (phonons). Strong carrier-carrier interactions can, in principle, open

a competing carrier relaxation channel, in which the excess energy of a hot conduction-band electron or a valence-band hole does not dissipate via electron-phonon scattering but is instead transferred to a valence-band electron, exciting it across the energy gap in a collision-like, impact-ionization event (**Figure 7a**). As a result, absorption of a photon produces not one but two e-h pairs; accordingly, this process is often referred to as CM. Strong motivation for CM studies has been provided by potential applications in PV technologies in which this effect can be utilized to increase power conversion efficiency of solar cells via increased photocurrent (37, 38, 78–81).

The ideal CM yield is described by a staircase function in which each increment of the incident photon energy by the band gap results in a new e-h pair, that is, the increase of quantum efficiency (QE) of photon-to-exciton conversion by 1 or 100% (**Figure 7b**, gray solid line). In the CM case, QE is greater than unity, and the value of $\eta = (\text{QE} - 1)$ defines the multiexciton yield. In bulk semiconductors, CM was first observed in the 1950s (82) and since then has been studied extensively both experimentally and theoretically. In contrast to the ideal staircase, the QE measured for bulk materials in the case of optical excitation typically exhibits a near linear growth above a threshold energy of $\hbar\omega_{\text{th}}$ (**Figure 7b**, red line). The inverse slope of this dependence represents a measure of the e-h pair creation energy ($\epsilon_{\text{eh}} = \Delta[(\text{QE})/\Delta(\hbar\omega)]^{-1} = [\Delta\eta/\Delta(\hbar\omega)]^{-1}$), which is the energy required to generate a new e-h pair at spectral energies above $\hbar\omega_{\text{th}}$. As indicated by a large body of experimental data (e.g., see Reference 83), the spectral threshold of CM and ϵ_{eh} are linked by the relationship $\hbar\omega_{\text{th}} = \epsilon_{\text{eh}} + E_g$.

On the basis of energy conservation alone, the minimal values of ϵ_{eh} and $\hbar\omega_{\text{th}}$ are E_g and $2E_g$, respectively (**Figure 7b**, blue dashed line). However, because of momentum conservation, a new e-h pair produced via impact ionization must carry nonzero kinetic energy. This results in an additional kinetic contribution (E_K) to ϵ_{eh} , which in the free-carrier approximation can be expressed as $E_K \approx 1.8E_g$ (84, 85). Phonon losses (E_{ph}) lead to a further increase in ϵ_{eh} by approximately 0.5 to 1.0 eV (84, 85). Given the above considerations, the e-h pair creation energy can be calculated from $\epsilon_{\text{eh}} = E_g + E_K + E_{\text{ph}}$, which implies that in bulk materials, ϵ_{eh} is at least $\sim 3E_g$, instead of the ideal value of E_g . Respectively, the CM threshold is at least $\sim 4E_g$, as compared with the energy-conservation-defined limit of $2E_g$ (**Figure 7b**, red solid line). For traditional PV

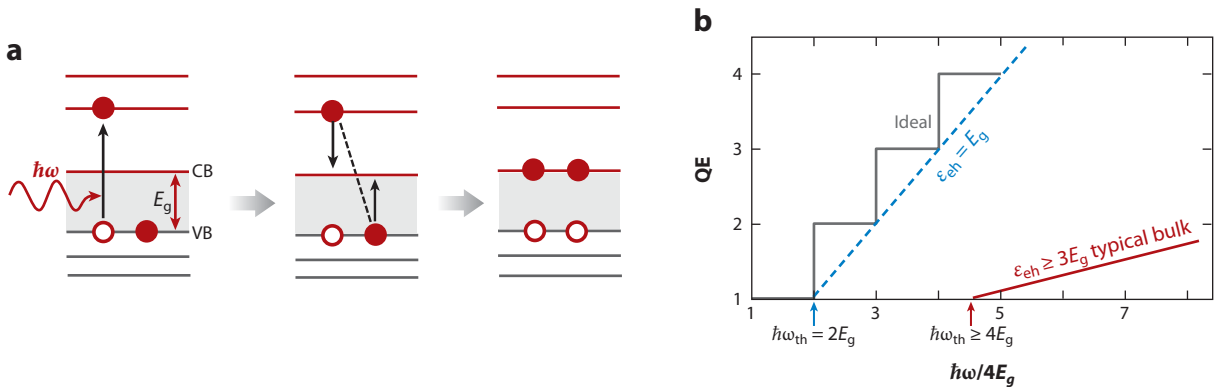


Figure 7

(a) A sequence of events involved in carrier multiplication. (*Left*) Absorption of a high-energy photon produces a hot conduction-band electron; (*middle*) this electron transfers its excess energy to the valence-band electron via an impact-ionization-like event, exciting it across the energy gap; (*right*) this leads to generation of a second e-h pair. (b) Ideal staircase-like quantum efficiency (QE) of photon to e-h-pair conversion observed in the energy-conservation-defined limit (solid gray line) in comparison to a more realistic semi-ideal linear dependence ($\epsilon_{\text{eh}} = E_g$; $\hbar\omega_{\text{th}} = 2E_g$; dashed blue line) and a typical dependence observed for bulk solids ($\epsilon_{\text{eh}} \geq 3E_g$; $\hbar\omega_{\text{th}} \geq 4E_g$; solid red line).

materials, such as Si, GaAs, and CdTe, with band gaps of 1.1 to 1.4 eV, the theoretical spectral onset of CM is near or above ~ 4 eV. Given that only a very small fraction of solar radiation is available at these energies, the benefits from CM in the case of bulk-semiconductor-based PVs are negligible.

As was suggested by Nozik (81), CM can be enhanced by using quantum-confined QDs. A wide separation between electronic states has been expected to suppress phonon losses leading to a reduced contribution from E_{ph} to the e-h pair creation energy (81). Further, previous studies of the effect of a varied E_g on Auger recombination (40), as well as the analysis of Auger lifetimes in QDs of direct- and indirect-gap semiconductors (41), strongly suggest that in the QDs, translational momentum is not conserved in carrier-carrier collision processes. This could, in principle, further reduce ϵ_{eh} by reducing E_k . These considerations have motivated recent renewed interest in CM with a focus on quantum-confined nanostructures.

The first experimental evidence for efficient CM in QDs was provided by spectroscopic studies of PbSe QDs reported by Schaller & Klimov in 2004 (32). An especially important result of this work was the observation of a considerable reduction of the CM threshold compared with bulk PbSe (to below $3E_g$), confirming a beneficial effect of quantum confinement on the CM process. Later, spectroscopic signatures of CM were observed for QDs of other compositions (86–90), including the important PV material Si (91, 92). Recent studies of QD solar cells have shown that CM can indeed produce greater-than-unity quantum efficiencies in photon-to-charge-carrier conversion (93), firmly establishing the relevance of this process to practical PV technologies.

3.2. Spectroscopic Measurements of Carrier Multiplication

As was proposed in the original report on CM in QDs (32), the efficiency of this process can be evaluated from the Auger decay signal of multiexcitons measured using either TA or time-resolved PL. In such measurements, multiexcitons are distinguished from single excitons on the basis of the significant difference in their recombination timescales (32). For example, in PbS and PbSe QDs, single-exciton lifetimes are on the order of hundreds of nanoseconds to microseconds, which means that in a typical ultrafast measurement limited to a few nanoseconds, the single-exciton signal is essentially constant. However, because of fast Auger recombination, multiexcitons have lifetimes of tens to hundreds of picoseconds and therefore are observed as a fast early-time component that decays to the single-exciton background (see Figure 8a).

In the case of TA measurements, one usually monitors the pump-induced bleach of the lowest energy 1S absorption feature ($\Delta\alpha_{1S}$) as, for example, in studies shown earlier in Figure 4b. The value of $\Delta\alpha_{1S}$ is directly proportional to the filling factor of the 1S state. In the case of PbS and PbSe QDs with a high, eightfold degeneracy of the 1S state, $\Delta\alpha_{1S}$ is also proportional to the total number of excitons residing in the QD, as in most of the practical situations realized experimentally the QD occupancy does not exceed eight. Thus, the amplitude of the 1S bleach immediately following excitation with a short pulse (usually referred to as a) represents a measure of the total number of excitons generated in the QD ensemble. Because of Auger recombination, multiexcitons originally produced via either multiphoton absorption or CM quickly decay to single excitons. As a result, the long-time signal that is measured following Auger recombination (b) is defined simply by the total number of photoexcited QDs. The average exciton multiplicity ($\langle N_x \rangle$), i.e., the average number of excitons per photoexcited QD, can be obtained from the ratio of a and b : $\langle N_x \rangle = a/b$. This quantity is of special importance in the case of CM studies, as its value measured in the limit of zero pump fluence (j) defines the QE of photon-to-exciton conversion, i.e., $\text{QE} = 1 + \eta = \lim_{j \rightarrow 0} \langle N_x \rangle = \lim_{j \rightarrow 0} (a/b)$ (94, 95).

The average exciton multiplicity can be related to the average QD occupancy $\langle N \rangle$ (introduced earlier) by $\langle N_x \rangle = \langle N \rangle / (1 - p_0)$, where p_0 is the fraction of unexcited ($N = 0$) QDs in the sample.

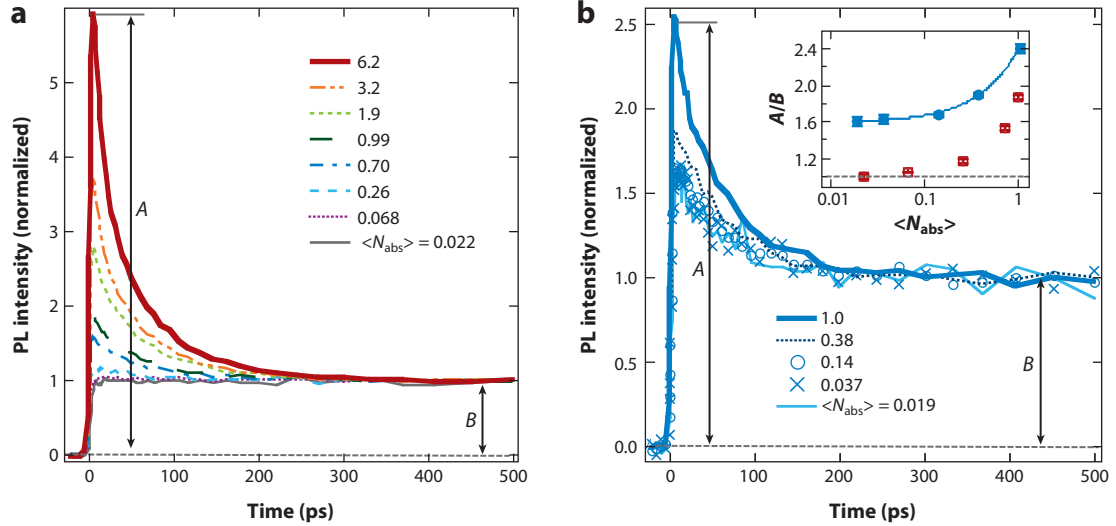


Figure 8

Time-resolved photoluminescence (PL) measurements of PbSe quantum dots (QDs), with $E_g = 0.795$ eV (vigorously stirred hexane solution). (a) Normalized PL traces recoded using excitation at 1.54 eV as a function of the average number of photons absorbed per dot per pulse ($\langle N_{\text{abs}} \rangle$). (b) Normalized PL traces recoded using excitation at 3.08 eV as a function of $\langle N_{\text{abs}} \rangle$. Inset: The A/B ratio as a function of $\langle N_{\text{abs}} \rangle$ for $\hbar\omega = 1.54$ eV [below the carrier multiplication (CM) threshold; red symbols] and 3.08 eV (above the CM threshold; blue symbols). The line is a fit to the 3.08 eV data, assuming Poisson photon absorption statistics. Adapted from Reference 96.

Without CM, the distribution of carrier populations across the QD ensemble immediately following excitation is Poissonian and $\langle N \rangle$ is simply equal to $\langle N_{\text{abs}} \rangle$, where $\langle N_{\text{abs}} \rangle = j\sigma$ is the average number of photons absorbed per QD per pulse and σ is the absorption cross section. This leads to the following expression for the exciton multiplicity: $\langle N_x \rangle = \langle N_{\text{abs}} \rangle / [1 - \exp(-\langle N_{\text{abs}} \rangle)] = j_p\sigma / [1 - \exp(-j_p\sigma)]$, which indicates that the low-intensity limit of $\langle N_x \rangle$ is unity and hence $\text{QE} = 1$, as expected in the regime without CM.

In the case of CM, the distribution of photon absorption events remains Poissonian; however, the resulting carrier distribution across the QD ensemble is non-Poissonian (95). To relate $\langle N_x \rangle$ to $\langle N_{\text{abs}} \rangle$ in this case, we consider the regime in which CM can produce no more than one additional exciton, and hence the multiexciton yield (i.e., in this case the probability of generating an additional e-h pair) is less than unity. In this situation, $\langle N \rangle = \sum_{m=0, \infty} p_m q_m$, where p_m is the Poisson probability of absorbing m photons and q_m is the average number of excitons generated in dots that absorbed m photons. When one photon is absorbed, the dot can have either a single exciton with probability $(1 - \eta)$ or a biexciton with probability η . As a result, $q_1 = (1 - \eta) + 2\eta = 1 + \eta$. If two photons are absorbed, there are three different possibilities: Both photons produce single excitons [probability $(1 - \eta)^2$], both produce biexcitons (probability η^2), and one produces an exciton and the other a biexciton [probability $2\eta(1 - \eta)$]. As a result, $q_2 = 2(1 - \eta) + 4\eta^2 + 1 + \eta = 2(1 + \eta)$. In general, $q_m = m(1 + \eta)$, and hence, $\langle N \rangle = (1 + \eta)\langle N_{\text{abs}} \rangle$. This further yields $\langle N_x \rangle = (1 + \eta)\langle N_{\text{abs}} \rangle / [1 - \exp(-\langle N_{\text{abs}} \rangle)]$ or, in terms of TA amplitudes,

$$a/b = \text{QE} \langle N_{\text{abs}} \rangle / [1 - \exp(-\langle N_{\text{abs}} \rangle)]. \quad 4.$$

In the regime of low excitation intensities when $\langle N_{\text{abs}} \rangle \ll 1$, one can only keep a term linear in $\langle N_{\text{abs}} \rangle$, which yields $\langle N_x \rangle = a/b \approx (1 + \eta)(1 + \langle N_{\text{abs}} \rangle/2) = \text{QE}(1 + j_p\sigma/2)$. This expression

indicates that QE can be directly inferred from pump intensity-dependent measurements of exciton multiplicity via linear extrapolation of $\langle N_x \rangle$ to zero fluence. Alternatively, one can employ the exact expression given by Equation 4 to fit experimental data and in this way derive QE.

Similar considerations can be applied in the analysis of PL time transients (48). One important distinction of PL from TA is that the PL intensity (I_{PL}) scales as a product of QD electron and hole occupancies. Therefore, the emission rate of a biexciton ($r_{\text{em}} = r_2$) is four times that of a single exciton: $r_2 = 4r_1$ (see Section 2.1). As a result, in the regime in which the CM yield is no greater than one, the early time PL signal is $A = (1 - \eta)r_1 + \eta r_2 = (1 + 3\eta)r_1$, whereas the amplitude of the long-time single-excitonic signal is $B = r_1$. On the basis of these relationships, $\eta = (A/B - 1)/3$ and $\text{QE} = (A/B + 2)/3$. This expression indicates that PL is a more sensitive probe of CM than TA, as the multiexciton-related component resulting from CM is amplified in PL threefold ($A/B - 1 = 3\eta$) compared with TA ($a/b - 1 = \eta$).

Figure 8 displays an example of CM measurements of PbSe QDs from Reference 96 that were conducted using femtosecond PL up-conversion (uPL), a technique in which subpicosecond temporal resolution is achieved by frequency mixing sample emission with an intense, variably delayed gating pulse in a nonlinear optical crystal. Figure 8a shows a series of time transients recorded using sub-CM threshold excitation at 1.54 eV, with different per pulse fluences that correspond to $\langle N_{\text{abs}} \rangle$ from 0.022 to 6.2. The high fluence traces show a pronounced initial fast component due to Auger recombination of multiexcitons, which results in an A/B ratio greater than unity. As the fluence is decreased, the A/B ratio decreases and approaches unity in the limit $\langle N_{\text{abs}} \rangle \rightarrow 0$ (inset of Figure 8b, red symbols). In the case of 3.08 eV excitation (Figure 8b), the overall signal behavior is similar. However, the low-intensity limit of the A/B ratio is greater than unity, indicating contributions from CM. The zero-fluence extrapolation of the measured A/B values (inset of Figure 8b, blue symbols) yields $\eta = 0.2$, which corresponds to $\text{QE} = 120\%$.

3.3. Effects of Photocharging

Early CM studies were mired in confusion, as a large spread in the QEs measured for nominally identical materials appeared in the literature (50, 89, 97–100). More recent investigations have established that those large discrepancies originated primarily from uncontrolled photocharging of QDs (48, 96). Common approaches to mitigating this problem involve the use of stirred (48, 50, 96, 97) (as in Figure 8) or flowed (101) QD solution samples, which prevents accumulation of long-lived charged species within the excitation volume. After eliminating these artifacts, photocharging-free measurements show good agreement between data sets obtained by different groups and/or different spectroscopic techniques (34, 48, 83).

The effect of charging on CM measurements is illustrated in Figure 9a, which compares PL time transients in a static versus a stirred sample. The static sample shows an increased early time signal and a decreased amplitude of the long-time slow background, which results in an apparent increase in the A/B ratio. This distortion is more pronounced at high pump intensities, but it persists in the limit of low fluences (Figure 9b) and eventually can result in the overestimation of the CM yield.

The role of charging on CM measurements was analyzed in great detail in Reference 48. The model used in this analysis is illustrated in Figure 9c. It compares a sequence of recombination events in the case of CM in a neutral (Figure 9c, top row) versus a charged (Figure 9c, bottom row) QD. A biexciton generated in a neutral QD decays via the Auger process to a single exciton. The corresponding emission rate, which defines the PL intensity, changes from $A = r_2 = 4r_1$ to $B = r_1$. The charged biexciton generated in a QD containing an excess electron is brighter than the neutral one, as it emits with the rate of $6r_1$. This charged biexciton first decays via Auger recombination to a charged exciton (trion) and then to a single nonemitting charge. These changes (an increase in the

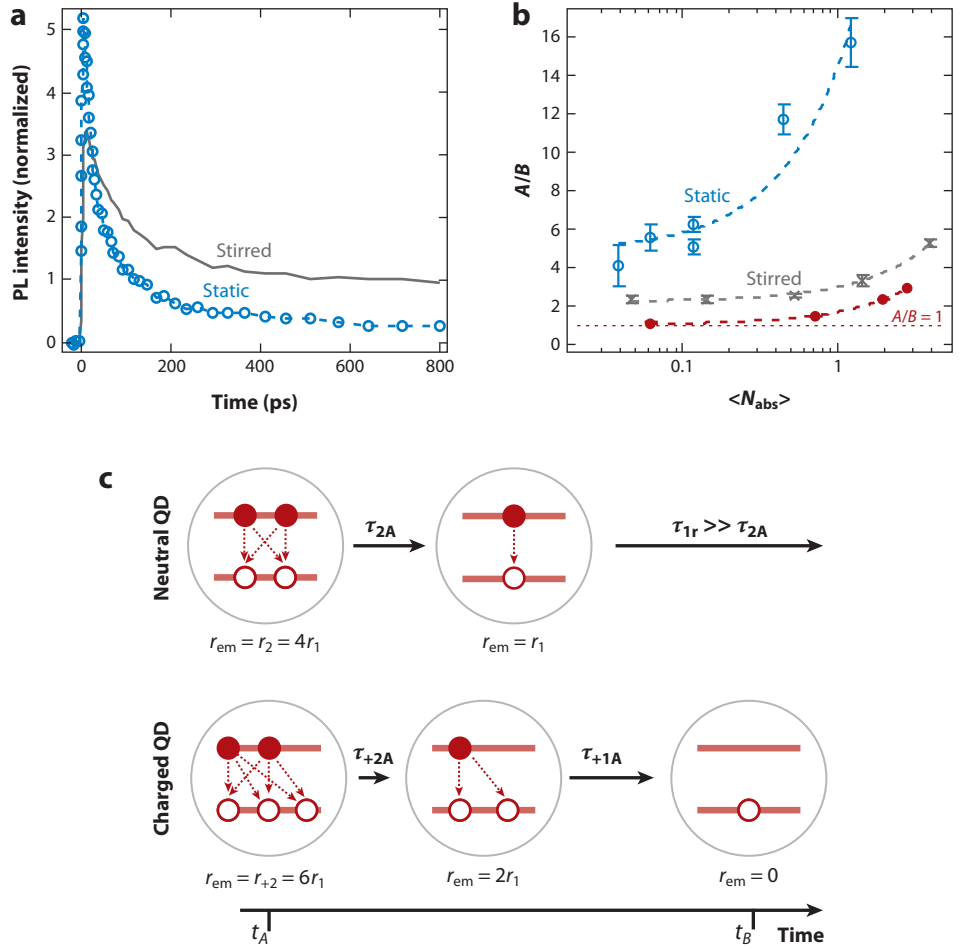


Figure 9

(a) Photoluminescence (PL) dynamics for static (circles) and stirred (black solid line) solutions of PbSe quantum dots (QDs) with $E_g = 0.63$ eV excited at 3.08 eV ($\langle N_{\text{abs}} \rangle = 1.4$). (b) The ratio of the early-to-late time PL signals (A/B) as a function of $\langle N_{\text{abs}} \rangle$ for 3.08 eV (gray crosses and blue circles are for stirred and static samples, respectively) and 1.54 eV (red circles) excitation. (c) Sequences of recombination events in the case of carrier multiplication in a neutral (top row) versus a charged QD (bottom row). Adapted from Reference 48.

early time signal accompanied by a reduction of the signal at late times) are consistent with signal distortions observed in the static sample. In fact, by using the degree of photocharging derived from independent measurements of band-edge absorption bleaching or PL quenching in a static sample, one can quantitatively relate the true CM yield measured on a stirred QD solution to the apparent yield inferred from the measurement of a static solution (48).

Recently, several reports have investigated the properties of charged states created via photoionization of PbSe and PbS QDs (53, 101, 102). The results of these studies have indicated that photoionization is especially pronounced at above band-edge excitation energies, suggesting that it occurs via ejection of a hot, unrelaxed charge. Further, the spectral dependence of the degree of photocharging revealed the existence of two photoionization thresholds ($\hbar\omega_i$) associated with onsets of weak ($\hbar\omega_{1i} \approx 1.5E_g$) and strong ($\hbar\omega_{2i} \approx 3E_g$) photocharging (102). These thresholds

were tentatively assigned to the 1P and 2P QD states, respectively. It was also determined that the probability of photocharging was fairly low, 10^{-4} to 10^{-3} per absorbed photon (102). However, the lifetime of the resulting charge-separated state was extremely long and characterized by tens-of-seconds timescales. As a result, a large fraction of the QDs in a photoexcited sample could cumulatively become charged even under the low-intensity excitation used in CM studies, leading to the distortion of CM signals. The fact that the spectral onset of strong photoionization scales with the band-gap energy and further is coincidentally near the CM threshold can be especially deceiving in experimental measurements. This emphasizes the importance of a careful analysis of the potential effects of photocharging on the results of spectroscopic studies of CM as well as CM studies involving photocurrent or photoconductive gain measurements.

3.4. Comparison to Bulk Semiconductors and Relation to Practical Photovoltaics

As was discussed earlier, one of the original motivations for investigation of CM in QDs was the expected enhancement of this effect due to strong quantum confinement. This enhancement has indeed been observed experimentally if one compares QD with bulk CM yields by referencing them to the relative photon energy normalized by E_g (34, 48, 83, 96). **Figure 10** shows a comparison of CM data for PbSe obtained by both ultrafast spectroscopy (**Figure 10**, blue symbols) (34, 83) and photocurrent measurements (green symbols) (93), while the QEs of bulk PbSe films (**Figure 10**, red symbols) were evaluated using ultrafast THz spectroscopy (103). From extrapolation of QD data to $QE = 1$, we find that the CM threshold is approximately $2.6E_g$, which is much lower than that in bulk PbSe films ($>7E_g$, according to Reference 103). Interestingly, the CM onset measured for QDs is also considerably smaller than the $4E_g$ minimum estimated by taking into account both energy and translation momentum conservation (84, 85) and instead is close to the limit defined by energy conservation alone. This is one of the predicted consequences of strong quantum confinement, which has been expected to lower the CM threshold due to relaxation of momentum conservation (40). Using the measured QEs one can estimate the e-h pair creation energy based on the difference in QEs measured for the same sample at two different photon energies. This procedure produces values from $2.3E_g$ to $3.25E_g$ (48), which are also lower than those measured for bulk PbSe films ($>4E_g$).

Although CM enhancement in QDs versus bulk is apparent when using normalized photon energies ($\hbar\omega/E_g$), the bulk CM yields appear to be higher than those in the QDs if analyzed in terms of the absolute values of $\hbar\omega$ without taking into account the confinement-induced increase in the band-gap energy (48). These considerations have led to the discussion of the validity of the $\hbar\omega/E_g$ representation in the analysis of CM yields as well as of the resulting conclusion on the CM enhancement in the QDs (97, 103). A convincing argument in favor of using the $\hbar\omega/E_g$ representation comes from a comparison of CM performance of two materials with different band gaps but the same ideal staircase-like QEs. In the absolute $\hbar\omega$ representation for any given photon energy, the material with a smaller E_g shows an apparent enhancement in the CM performance compared with a larger-gap material (**Figure 10b**). This assessment is obviously not accurate (both materials are ideal multipliers), and it is a direct consequence of neglecting the difference in the band-gap energies. On a normalized energy scale, both materials show the same QEs (**Figure 10c**), which immediately leads to the correct assessment that they are identical with regard to their CM performance.

It is noteworthy that the practice of using the $\hbar\omega/E_g$ scale in the analysis of CM data derives from the earliest studies of bulk semiconductors. Even then, it was already acknowledged that the band-gap energy represents the intrinsic energy scale of the CM process, and specifically that both ε_{eh} and $\hbar\omega_{th}$ are directly linked to the band-gap energy (84, 85) by proportionality factors that are ideally close to 3 and 4, respectively.

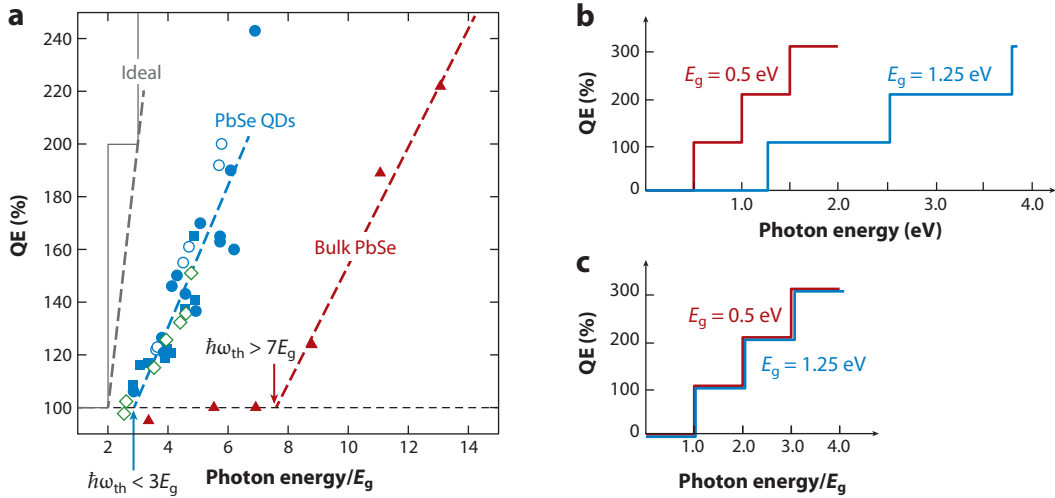


Figure 10

(a) Quantum efficiencies (QEs) of photon-to-exciton conversion in PbSe quantum dots (QDs) versus those of bulk PbSe films (red triangle) (103) as a function of $\hbar\omega/E_g$; the QD data were obtained via several complementary techniques: transient absorption (blue solid circle, blue open circle; data from References 34 and 83, respectively), transient photoluminescence (blue square) (34), and photocurrent measurements (green diamond) (93). The carrier multiplication (CM) threshold ($\hbar\omega_{th}$) in the PbSe QDs is greatly reduced compared with bulk PbSe. Ideal cases set by energy conservation are shown by a solid gray line (ideal staircase) and a dashed gray line (more realistic dependence with $\epsilon_{ch} = E_g$ and $\hbar\omega_{th} = 2E_g$). Adapted from Reference 34. (b) QEs of two ideal CM materials with different band gaps (0.5 eV and 1.25 eV) plotted as a function of the absolute photon energy $\hbar\omega$. (c) QEs of the same materials as in panel b but plotted as a function of the normalized photon energy $\hbar\omega/E_g$.

The analysis of the PV performance of CM-exhibiting materials also suggests that the CM-related enhancement in the PV conversion efficiency is controlled not by the absolute values of the CM threshold and the e-h creation energy but by the proportionality factors that relate these quantities to the band-gap energy (37, 38, 83). Specifically, the closer $\hbar\omega_{th}$ and ϵ_{ch} come to $2E_g$ and E_g , respectively, the stronger the PV performance. According to detailed balance calculations, the thermodynamic limit of a single-junction PV in the absence of CM is $\sim 31\%$ (104). In the case of CM described by the ideal staircase-like QE (Figure 7b, gray line), this limit is increased to 43%–45% (37, 80). However, a more common situation realized in both bulk and QD systems is a linear growth of QE with $\hbar\omega$ beyond the onset at $\hbar\omega_{th}$, with an inverse slope defined by ϵ_{ch} (Figures 7b and 10a). In the case when $\hbar\omega_{th}$ and ϵ_{ch} are limited just by energy conservation ($\epsilon_{ch} = E_g$ and $\hbar\omega_{th} = 2E_g$; Figure 7b, dashed blue line), CM still produces a considerable improvement in power conversion efficiency, which can reach $\sim 37\%$ (83). However, the CM-related gains quickly decrease with increasing numerical prefactors in ϵ_{ch} and $\hbar\omega_{th}$. Specifically, for experimentally observed values of ϵ_{ch} of approximately $2E_g$ to $3E_g$ and $\hbar\omega_{th}$ of $\sim 2.6E_g$, the power conversion efficiency shows only a marginal increase due to CM of up to 1%.

3.5. Window-of-Opportunity Carrier Multiplication Model

The above discussion of CM results for PbSe QDs, as well as the analysis of published CM data for other materials, indicate that even in nanostructures with the strongest CM performance, such as PbSe nanorods (105, 106) and Si QDs (91, 107, 108), the QE of photon-to-exciton conversion within the PV-relevant spectral range is still not sufficiently high to appreciably increase power

conversion efficiency of practical devices (37, 38). This highlights the need for new nanostructures tailored to enhance CM for energies relevant to solar energy conversion. One complication in the development of such materials is the lack of an established theory for treating this process in quantum-confined nanoparticles. For example, in addition to traditional impact ionization models (109–114), there have been a number of other approaches that rely on specific physics of strongly confined nanostructures, including quantum-mechanical superposition of single-exciton and biexciton states (115, 116), direct photogeneration of multiexcitons via virtual single-exciton and biexciton states (94, 117–120), and quantum cutting of an incident photon to produce two excitons in adjacent NCs (92, 121).

To facilitate the search for new, more efficient CM materials, recently Reference 122 proposed an experiment-inspired window-of-opportunity model of CM, which treats this process in terms of a competition between impact-ionization-like scattering and non-CM energy losses. An important feature of this model is that it allows one to relate a key CM parameter, the e-h pair creation energy, to two easily measurable quantities: the biexciton Auger lifetime and the rate of carrier relaxation at near band-edge energies, which are used, respectively, as surrogates for the characteristic time of an individual CM event and the rate of cooling processes competing with CM.

In order to resolve ε_{eh} into its constituent mechanisms (i.e., the processes responsible for CM and non-CM energy losses), we consider the situation in which the material is excited slightly above the CM threshold. In this case, the relaxation time window (T) available for CM (window of opportunity) (Figure 11a) is short compared with the timescale of the individual CM event (τ_{CM}), and the multiexciton yield (or CM yield) can be estimated from $\eta = \text{QE} - 1 = T/\tau_{\text{CM}}$. This can be further rewritten as $\eta = (E_{\text{exc}} - E_{\text{th}})/(k_{\text{cool}}\tau_{\text{CM}})$ if we express T in terms of the energy of a hot photoexcited carrier (E_{exc}) minus the minimal carrier energy required to initiate CM (E_{th}) and divided by the energy-loss rate during intraband cooling (k_{cool}). Given that photoexcitation produces both an electron and a hole, the total multiexciton yield is a sum of contributions due to both carriers: $\eta = \eta_{\text{e}} + \eta_{\text{h}}$. Assuming that τ_{CM} , k_{cool} , and E_{th} are similar for electrons and holes (a reasonable assumption for the IV–VI semiconductors considered here as they are characterized by mirror-symmetric conduction and valence bands), we can present the CM yield as $\eta = (E_{\text{exc}} - \hbar\omega_{\text{th}})/(k_{\text{cool}}\tau_{\text{CM}})$. From this relationship, $\varepsilon_{\text{eh}} = d(\hbar\omega)/d\eta = k_{\text{cool}}\tau_{\text{CM}}$, which indicates that ε_{eh} is defined by the competition between CM and carrier cooling and suggests that a reduction in ε_{eh} (i.e., an increase in QE) can be achieved by reducing either k_{cool} or τ_{CM} , or both. The above simplified treatment, which has assumed a near-threshold excitation of CM (i.e., a single CM event), can be generalized for the situation of an arbitrary excess energy of a photoexcited carrier when multiple CM events are possible (Figure 11b). Analytical and Monte Carlo approaches for such generalization were discussed in Reference 122. Both of these approaches allow for an accurate description of experimentally measured CM yields as illustrated in Figure 11b for PbSe QDs.

3.6. Effect of Quantum Dot Size

We first apply a window-of-opportunity model to rationalize the observed size-dependent trends in CM. These trends can be inferred from the variation in the CM yields measured for a fixed excitation energy for QDs of different sizes and, therefore, different band-gap energies. An example of such measurements is shown in Figure 11b (red symbols) using a plot of QE versus normalized photon energy, $\hbar\omega/E_{\text{g}}$. In this representation, the experimental data show an approximately linear growth, which suggests the following scaling for the multiexciton yield: $\eta \propto (\hbar\omega/E_{\text{g}} - \alpha)$, where α is a constant relating $\hbar\omega_{\text{th}}$ to E_{g} ($\hbar\omega_{\text{th}} = \alpha E_{\text{g}}$; for PbSe QDs α is approximately 2.6). Given that ε_{eh} is defined by $(d\eta/d\hbar\omega)^{-1}$, the observed scaling suggests that ε_{eh} is directly proportional to E_{g} : $\varepsilon_{\text{eh}} = \beta E_{\text{g}}$, where β is a size-independent constant. Although this is

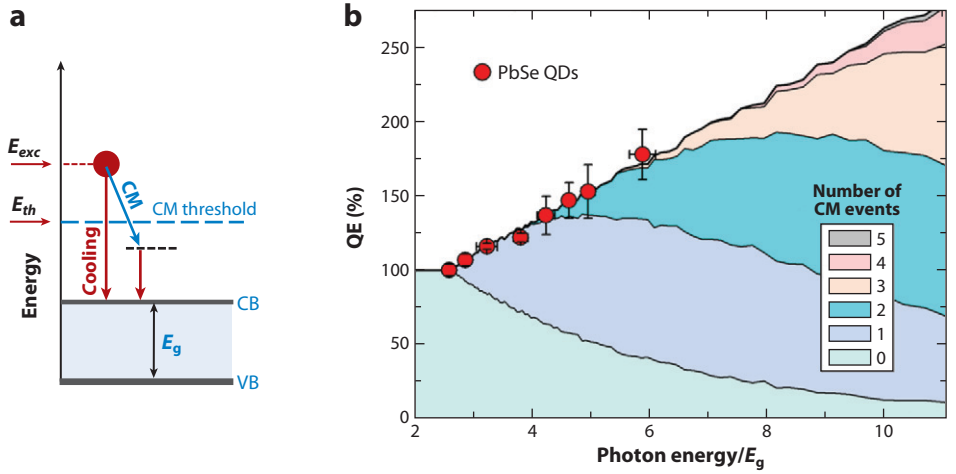


Figure 11

(a) In the window-of-opportunity model, carrier multiplication (CM) yields are defined by the competition between impact-ionization-like events, producing new e-h pairs (characteristic time constant τ_{CM}) and non-CM energy losses (energy loss rate k_{cool}). (b) Quantum efficiencies (QEs) of photon-to-exciton conversion measured for PbSe QDs of various sizes (red circles; 3.1 eV excitation) are modeled using Monte Carlo calculations (solid jagged lines). The shaded filling indicates that QE is composed of different orders of CM events (i.e., zero, one, two, etc., additional excitons produced via CM). Adapted from Reference 122. Abbreviations: CB, conduction band; VB, valence band.

functionally similar to the trend observed in bulk semiconductors, where β is at least 3, in QDs this seemingly simple scaling likely arises from a complex interplay between correlated size-dependent changes in the CM rate and the rate of competing non-CM energy losses, as discussed below.

To rationalize the observation of direct scaling of ϵ_{eh} with E_g , studies found in Reference 34 analyzed size-dependent trends expected for τ_{CM} and k_{cool} . Because direct measurements of τ_{CM} are not straightforward, it was suggested that the time constant of biexciton Auger recombination (τ_{2A}) can be used as a surrogate for τ_{CM} . As was discussed earlier, biexciton Auger decay is the inverse of CM, and, therefore, both processes are described by the same Coulomb matrix element. However, because of the involvement of different densities of final states (single exciton in the case of Auger decay and biexcitons in the case of CM), τ_{2A} is proportional rather than equal to the characteristic CM time. Therefore, the measurements of Auger decay do not provide an absolute value of τ_{CM} but only allow for evaluation of relative changes in the CM time constant between QDs of different sizes or different compositions.

As was pointed out previously, Auger lifetimes in QDs exhibit a universal linear scaling with the QD volume (V -scaling) (31, 41). Interestingly, not only the size dependence but also the Auger lifetimes themselves are very similar across similarly sized QDs of different compositions, including both direct- and indirect-gap materials (41), despite vastly different Auger constants in their bulk form (123). These universal trends likely derive from the relaxation of momentum conservation, which diminishes the role of the exact band structure in Auger recombination.

The direct relation between CM and Auger decay suggests that CM time constants also decrease with decreasing QD size, suggesting that this process is enhanced in smaller NCs (42). However, given that ϵ_{eh} is defined by the product of τ_{CM} and k_{cool} , the overall effect of QD size on multiexciton yields also depends on the size dependence of the non-CM cooling rate.

As was proposed in References 34 and 122, the relative changes in k_{cool} due to variation in QD size or composition can be evaluated using standard measurements of carrier relaxation between the two adjacent band-edge 1P and 1S states ($k_{1\text{P}1\text{S}}$) (124). Although the absolute values of the rate measured in this way may differ from those at higher, more CM-relevant energies, they can still be used as a surrogate for τ_{CM} because it is unlikely that the size- or composition-dependent trends at high carrier energies are different from those at lower energies.

Early studies of CdSe QDs indicated that $k_{1\text{P}1\text{S}}$ scales inversely with the QD volume, that is, $k_{1\text{P}1\text{S}} \propto R^{-3}$ (29, 125). More recent measurements indicate that a similar scaling also holds for PbSe NCs (124). Further, both materials exhibit a similar V -scaling (i.e., as R^3) of Auger lifetimes. These considerations suggest that the product of $k_{1\text{P}1\text{S}}$ and $\tau_{2\text{A}}$ is size independent, which may itself be another universal trend for QDs. Combining this observation with the previous expression for ε_{eh} , we find that $\varepsilon_{\text{eh}} = k_{\text{cool}}\tau_{\text{CM}} = \rho k_{1\text{P}1\text{S}}\tau_{2\text{A}}$, where ρ is a coefficient that accounts for the effect of densities of exciton and biexciton states (34). Given the size independence of $k_{1\text{P}1\text{S}}\tau_{2\text{A}}$, the size-dependent trends observed for ε_{eh} are likely derived from the size or E_{g} dependence of ρ . Specifically, direct scaling of ε_{eh} with E_{g} suggests that ρ is also likely linear in E_{g} .

3.8. Effect of Nanocrystal Shape

Recent studies of elongated NCs, or nanorods (NRs), suggest that one promising approach to enhancing CM efficiency is through shape control, which might allow manipulation of τ_{CM} by manipulating the strength of carrier-carrier Coulomb coupling (105, 106). **Figure 12a** shows a plot of QEs measured for PbSe NRs of various aspect ratios (colored symbols) in comparison to those for spherically shaped QDs (gray symbols). A general trend seen for the NRs, namely the increase in QE with increasing $\hbar\omega/E_{\text{g}}$, is similar to that observed for the QDs. However, for a given $\hbar\omega/E_{\text{g}}$, the NR data show a significant spread, indicating that in addition to the NR E_{g} (defined primarily by its radius), the NR length is also an important parameter in the CM process.

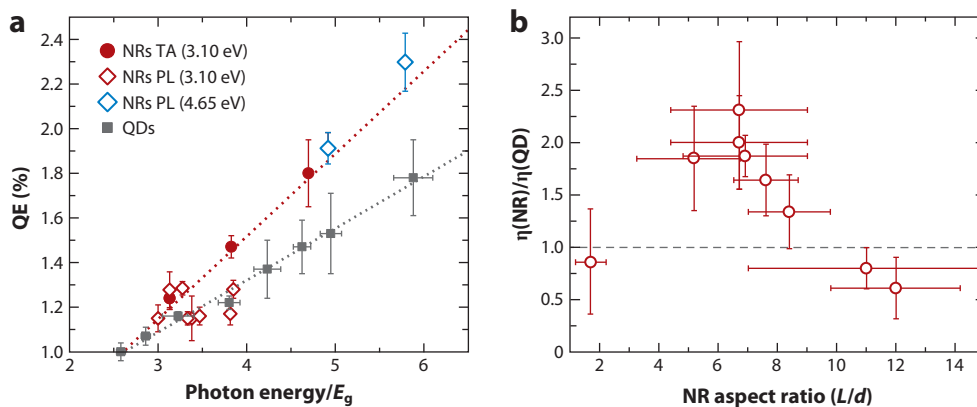


Figure 12

(a) Quantum efficiencies (QEs) of photon-to-exciton conversion for a series of PbSe nanorods (NRs) with various diameters and aspect ratios measured using excitation either at 3.1 eV [red solid circles and red open diamonds are transient absorption (TA) and transient photoluminescence (PL) measurements, respectively] or 4.65 eV (blue open diamonds) plotted as a function of $\hbar\omega/E_{\text{g}}$. The NR results are compared with literature values for PbSe quantum dots (QDs) (gray solid squares). (b) The carrier multiplication-yield enhancement factors for NRs versus QDs with similar band gaps as a function of NR aspect ratio. Adapted from Reference 106.

A significant dependence of CM performance on degree of elongation is illustrated in **Figure 12b**, where multiexciton yields of NRs normalized by those of QDs of the same E_g are plotted as a function of the NR aspect ratio defined as the ratio of the NR length (L) to its diameter (d). These data show a progressive increase in the CM enhancement factor for NRs over QDs with increasing L/d , which reaches 2–2.3 for aspect ratios of approximately 7. Further elongation leads to a gradual decrease of the QE, first down to values typical of the QDs and then even below those. From the QEs measured for a fixed excitation energy (3 eV) for NRs with varied E_g and near-optimal aspect ratios, the size-averaged ($\langle \epsilon_{eh} \rangle$) e-h pair creation energy is $2.7E_g$ (106) (**Figure 12a**, red dotted line), which is a considerable improvement over $\langle \epsilon_{eh} \rangle = 4.3E_g$ observed for PbSe QDs.

An intriguing observation made in Reference 106 was that NC elongation has opposite effects on CM and Auger recombination efficiencies. On the basis of recent studies (126), PbSe QDs and NRs exhibit similar intraband dynamics, suggesting similar k_{cool} rates. This implies that the CM enhancement observed in NRs with moderate elongation is likely derived from shortening of the CM time constant. This conclusion seems to suggest that Auger lifetimes should also become shorter upon elongation. However, the τ_{2A} time constants for PbSe NRs are known to be systematically longer than those for the PbSe QDs (106). To explain this apparent discrepancy, Reference 106 invoked the difference in the character of high- and low-energy excitations in the NRs. Owing to strong e-h attraction typical of 1D semiconductors, band-edge electrons and holes in the NRs are Coulombically bound into tightly confined excitons (127, 128). As a result, Auger recombination becomes less efficient than in the QDs, as it occurs via two-particle collisions of weakly interacting charge-neutral excitons (127, 129, 130). The situation, however, is different in the case of CM, which involves hot, unrelaxed charges before they form bound excitonic states. In this way, the CM mechanism in NRs is likely similar to that in the QDs, but it is mediated by a stronger Coulomb interaction, which is enhanced due to reduced dielectric screening and the 1D character of electronic states (127, 128).

3.9. Effect of Competing Energy-Loss Channels

In addition to τ_{CM} , an important parameter that directly affects multiexciton yields is the rate of energy-loss processes competing with CM. An observation of direct correlation between the intraband relaxation rates and multiexciton yields was first reported in Reference 131 via studies of CM and Auger recombination in PbS and PbSe QDs. As expected on the basis of universal V-scaling of Auger lifetimes, QDs of both compositions exhibited comparable values of τ_{2A} (**Figure 13a**), and hence presumably similar CM time constants. However, the measured CM yields were considerably higher in PbSe QDs than in PbS QDs (**Figure 13b**). These observations were rationalized by linking the observed difference in the QEs to the difference in energy losses due to phonon emission estimated from the product of the constant of a polar carrier-phonon coupling (α_{pol}) and the energy of an LO phonon ($\hbar\omega_{LO}$): $k_{cool} \propto \alpha_{pol}\hbar\omega_{LO}$. On the basis of these estimations, k_{cool} was expected to be approximately 2.5 times larger in PbS QDs than in PbSe QDs. Owing to direct proportionality between ϵ_{eh} and k_{cool} , this should translate into a factor of ~ 2.5 difference in the e-h pair creation energies. Because of this considerably greater value of ϵ_{eh} , the PbS QDs were expected to produce smaller multiexciton yields, as was indeed observed experimentally.

In Reference 122, these studies were extended to include PbTe QDs. Additionally, the estimations of expected k_{cool} rates based on bulk-material parameters were validated via direct measurements of intraband cooling conducted by analyzing 1P-to-1S relaxation. The results of these studies are illustrated in **Figure 13c**, which compares buildup dynamics of the 1S band-edge bleach in PbTe and PbS QDs of similar band-gaps (0.86 eV) excited with 1.5 eV, 50-fs pulses. This buildup is significantly slower in PbTe QDs, indicating slower intraband cooling. To quantify

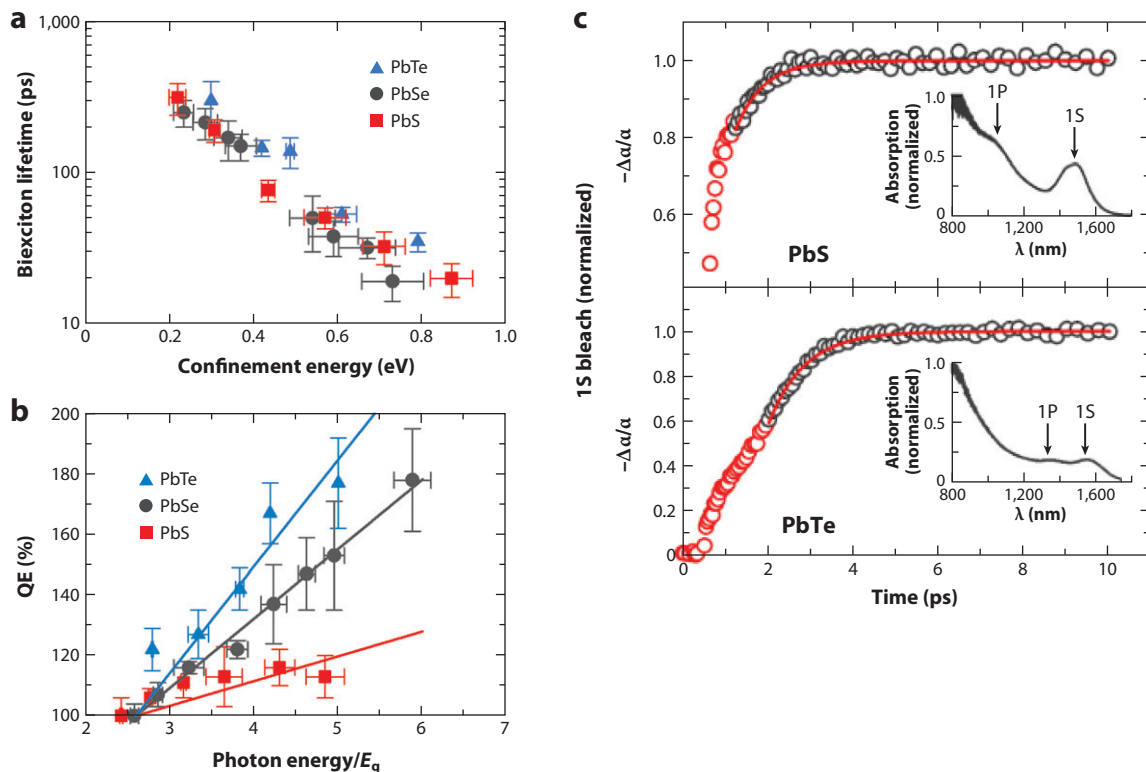


Figure 13

(a) Biexciton Auger lifetimes for PbS, PbSe, and PbTe quantum dots (QDs) plotted as a function of confinement energy defined as the difference between the band gaps of the QDs and the parental bulk semiconductor. The similarity of Auger time constants among the three compositions suggests the similarity of the characteristic carrier multiplication (CM) times. (b) Quantum efficiencies (QEs) of photon-to-exciton conversion for PbTe (blue triangle), PbSe (gray circle), and PbS (red square) QDs as a function of $\hbar\omega/E_g$ for differently sized QDs measured with excitation at 3.1 eV. Despite similar Auger time constants in panel a, these materials show strikingly different CM yields arising from the difference in the non-CM energy relaxation rates. (c) The buildup of the 1S bleach in PbS (top) and PbTe (bottom) QDs measured by transient absorption. The red data points represent the instantaneous Coulomb shift due to hot carriers; it is followed by slower growth due to population transfer from the 1P to the 1S state. The 1S-1P energy separation (ΔE_{1S1P}) is derived from the absorption spectra (insets). Slower intraband relaxation in PbTe versus PbS QDs results in increased CM yields (see panel b). Adapted from References 34 and 122.

the difference between the two materials, one can estimate a near-band-edge energy-loss rate (k_{1P1S}) from the ratio of the 1S-1P energy separation (ΔE_{1P1S} ; insets in Figure 13c) and the exponential time constant of the 1S bleach buildup (τ_{1P1S}). On the basis of intraband relaxation studies that included all three compounds (PbS, PbSe, and PbTe), $k_{1P1S}(\text{PbTe}):k_{1P1S}(\text{PbSe}):k_{1P1S}(\text{PbS}) \approx 1:2.0:4.2$. Together with the expected similarity between the τ_{CM} time constants, these results suggest a progressive increase in the CM yields from PbS to PbSe and then to PbTe. The CM measurements agreed with this prediction (Figure 13b). In fact, analysis of the slopes of the measured QE versus dependences indicated that the relationship between the e-h pair creation energies (1:1.8:4.5 for PbTe, PbSe, and PbS QDs, respectively) is in close agreement with that observed for the measured 1P-1S cooling rates. This once again validates a phenomenological window-of-opportunity model, which directly relates the e-h pair creation energies to τ_{CM} and k_{cool} .

3.10. Enhanced Carrier Multiplication via Intraband Cooling-Rate Engineering

On the basis of observations in References 122 and 131, which suggest a significant effect of competing energy loss channels on the overall multiexciton yield, one might attempt to design a nanostructure with slowed intraband cooling for enhancing CM. An example of such a structure is shown in **Figure 14a** (C. Cirloganu, L.A. Padilha, Q. Lin, N. Makarov, K.A. Velizhanin, H. Luo, I. Robel, J.M. Pietryga, and V.I. Klimov, unpublished results). It represents a hetero-QD in which a PbSe core is overcoated with an especially thick CdSe shell. Owing to a small conduction-band offset between CdSe and PbSe, the electron wavefunction ($1S_e$) in these QDs occupies the entire volume of the core-shell structure, whereas the band-edge hole wavefunction ($1S_h$) is tightly confined

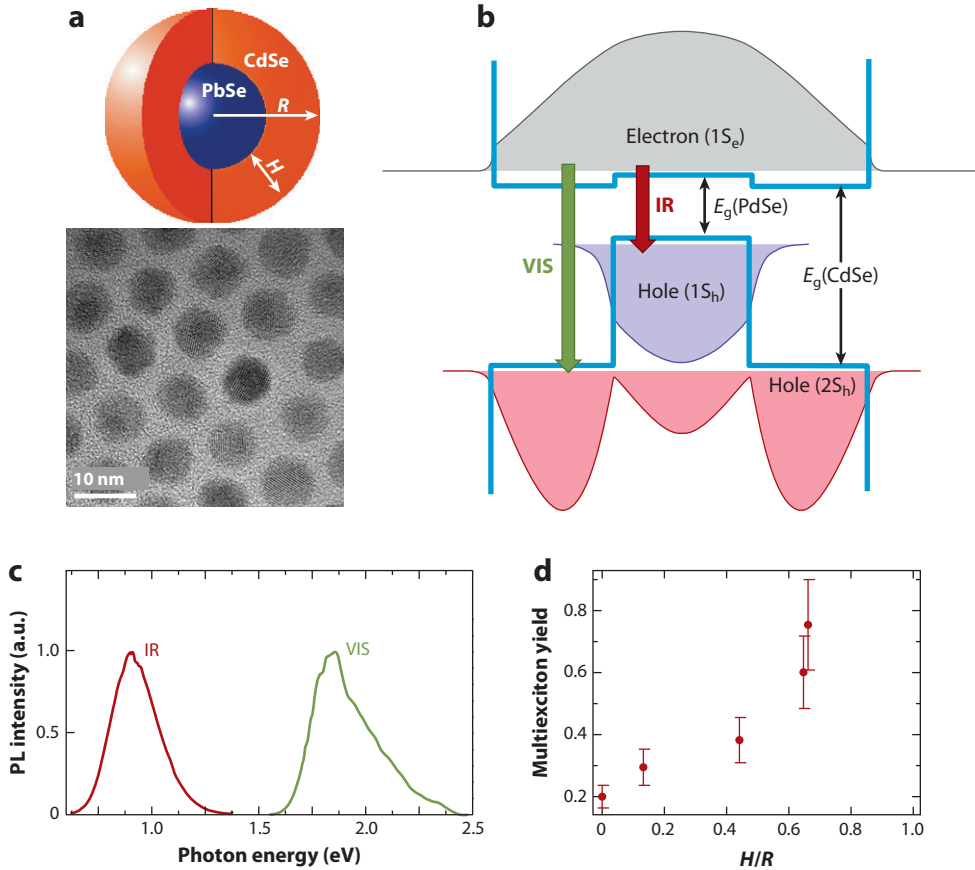


Figure 14

(a) Schematic illustration of the structure of PbSe/CdSe core-shell quantum dots (QDs), along with a transmission electron microscopy image of the sample with a core radius of 1.8 nm and shell thickness (H) of 2.2 nm ($H/R = 0.55$; R is the total radius). (b) An approximate band diagram of PbSe/CdSe QDs with the spatial distribution of the electron $1S_e$ (gray shading) and the hole $1S_h$ (purple shading) and $2S_h$ (light-red shading) wave functions. Green and dark red arrows show, respectively, optical transitions responsible for visible (VIS) emission from the shell and infrared (IR) emission from the core. (c) A two-band emission spectrum of these QDs measured with 3-eV excitation; the bands are independently normalized to have the same peak intensity. The IR band corresponds to the optical transition involving the core-localized hole, whereas the VIS band is due to the optical transition involving the shell-localized hole (see panel b). (d) Multiexciton yield as a function of H/R for samples with similar band-gap energies of ~ 0.89 eV. Abbreviation: PL, photoluminescence.

to the core because of the large confinement potential at the core-shell interface (**Figure 14b**). A typical signature of a large mismatch of effective volumes occupied by electrons and holes is reduced e-h overlap and consequently slowed single-exciton lifetimes. Indeed, as the CdSe shell thickness is increased, the measured PL lifetime becomes longer. However, the most striking effect of increasing shell thickness is the development of a second emission band in the visible range, which is observed simultaneously with the infrared band (**Figure 14c**). Analysis of the electronic states in these QDs using effective mass calculations suggests that the visible band arises from transitions that couple the $1S_e$ electron level to the $2S_h$ hole state localized primarily in the CdSe shell region of the QD (**Figure 14b**). Thus, this band represents hot emission due to recombination of an unrelaxed hole with a relaxed band-edge electron. Normally, because of extremely fast intraband relaxation, hot emission in QDs can only be observed using ultrafast spectroscopic measurements. The fact that in these structures hot shell-related PL is observed under low-intensity continuous wave excitation suggests a dramatic slowing down in intraband relaxation compared with standard QDs. This further suggests a dramatic decrease in the k_{cool} rate, which should result in increased multiexciton production.

The expected enhancement in the CM yield was indeed observed experimentally by studying a series of samples with a fixed overall radius (R up to 5 nm) and progressively increasing thickness of CdSe shell (the H/R ratio up to 0.7) grown via a cation exchange method. It was observed that visible PL, which signals the attainment of the regime of slowed cooling, developed fairly sharply when H/R became greater than ~ 0.5 . This was accompanied by a quick growth of the CM yield. The effect was especially pronounced in a series of core-shell samples with similar band gaps but different H/R ratios. An example of CM measurements for such a series with E_g of ~ 0.89 eV is given in **Figure 14d**; excitation at 3.1 eV in this case corresponds to $\hbar\omega/E_g \approx 3.5$. The core-only sample shows a multiexciton yield of 20%. In a core-shell sample with a thin shell ($H/R = 0.13$), η increases to 29% and then to 38% for a sample with $H/R = 0.44$. When H/R exceeds 0.4–0.5, CM yield exhibits an especially large increase. For example, in the sample with $H/R = 0.7$, η reaches 75%, which is almost 4 times greater than in the core-only sample. These results indicate the large promise of cooling-rate engineering for enhancing CM, perhaps, up to the limit defined by energy conservation.

SUMMARY POINTS

1. This article has provided an overview of recent progress in the understanding of multicarrier phenomena in quantum-confined colloidal NCs with focus on Auger recombination and CM. There has been growing realization that the role of multicarrier processes in NCs is greatly enhanced compared with parental bulk solids, which is a combined result of factors such as close proximity between interacting charges, reduced dielectric screening, and relaxation of restrictions associated with translational momentum conservation.
2. Due to strong quantum confinement, which leads to mixing between different states, the importance of details of a specific band structure, such as the band-gap energy or direct-versus-indirect character of the band gap, is greatly diminished in NCs, which leads to the development of universal size-dependent trends in multicarrier processes. One such trend is direct scaling of multiexciton Auger lifetimes with NC volume (sometimes referred to as V -scaling), which was first observed in CdSe QDs (31) and then confirmed for QDs of many other compositions (41).
3. An important result of recent studies of Auger effects is the observation of a breakdown of V -scaling in core-shell structures with an especially thick shell, which exhibited

considerably greater suppression of Auger decay than can be accounted for based on the QD volume. This observation highlighted the important role of NC interfaces in Auger recombination, as was first predicted by theoretical calculations (71). According to these calculations, by smoothing the interfacial potential one can suppress Auger decay by reducing the strength of the intraband transition by which the energy accepting charge is excited in the course of Auger recombination. The power of interface engineering for controlling Auger recombination has been demonstrated by recent studies of the effect of intentional alloying of CdSe/CdS QD core-shell interfaces on multicarrier recombination in the case of both neutral and charged excitations (66, 75) as well as on the performance of QD-LEDs (76).

4. Some of the insights gained from studies of Auger recombination are directly applicable to the inverse process of CM. Specifically, previous observations of a universal V -scaling of Auger lifetimes suggest that the characteristic CM time only weakly depends on NC composition and is primarily defined by the QD size. This implies that the variations in CM yields between similarly sized QDs of different compositions likely relate to a difference in the rate of competing energy relaxation mechanisms, such as phonon emission. This assessment has been confirmed by comparative studies of the CM performance of QDs of PbS, PbSe, and PbTe conducted in conjunction with studies of Auger decay and intraband cooling (122, 131).
5. A useful quantity for characterizing the CM performance of a given material is the e-h pair creation energy (ϵ_{eh}), which defines the energy increment required to generate a new e-h pair above the CM threshold. This quantity directly accounts for the competition between impact-ionization-like events that produce new excitons and non-CM intraband relaxation. On the basis of the window-of-opportunity model (122), ϵ_{eh} can be calculated from the product of the non-CM energy-loss rate (k_{cool}) and the characteristic time of an individual CM event (τ_{CM}). The use of ϵ_{eh} provides a useful tool for predicting the CM performance of a material on the basis of fairly straightforward measurements of biexciton Auger lifetimes and near-band-edge intraband cooling rates, which are used as proxies for τ_{CM} and k_{cool} , respectively (34, 122).
6. A universal material-independent size dependence of τ_{CM} , expected based on a universal V -scaling of multiexciton Auger lifetimes, along with size-dependent trends observed for intraband cooling, leads to an almost linear scaling of ϵ_{eh} with the QD band-gap energy: $\epsilon_{eh} = \beta E_g$. As demonstrated by experimental studies (34, 122), the material-dependent variations in the proportionality factor β are primarily linked to the difference in non-CM energy losses likely associated with electron-phonon scattering. This suggests that with standard monocomponent QDs, one has only limited control over CM performance, mostly accomplished by selecting materials with a weaker electron-phonon coupling.
7. One approach for enhancing multiexciton production is provided by shape control. As was shown in References 105 and 106, by using PbSe NRs with a moderate elongation (aspect ratio of ~ 7) one can achieve an approximately twofold increase in the CM yield over spherical QDs, which was attributed to enhanced Coulomb interactions, leading to an increased rate of CM events. An additional tool for tuning CM performance is the use of heterostructures, such as PbSe/CdSe core-shell QDs with especially thick shells, designed to slow down intraband cooling. In addition to core-related infrared emission, these QDs also exhibit visible PL associated with radiative recombination of hot holes residing in the shell. This indicates a dramatic reduction in the hole cooling rate, which in principle should reduce ϵ_{eh} and thus enhance CM performance. These structures indeed

demonstrate a considerable, almost fourfold increase in the CM yield compared with core-only PbSe QDs. Further enhancements in the CM performance, potentially up to the energy-conservation-defined limit, should be possible through combining optimal low-phonon-loss compositions with shape control and internal-structure engineering.

DISCLOSURE STATEMENT

The author is not aware of any affiliations, memberships, funding, or financial holdings that might be perceived as affecting the objectivity of this review.

ACKNOWLEDGMENTS

Carrier multiplication studies discussed in this article were supported by the Center for Advanced Solar Photophysics (CASP), the Energy Frontier Research Center funded by the Office of Basic Energy Sciences (OBES) of the Office of Science (OS) of the US Department of Energy (DOE). The studies of Auger recombination were supported by the Chemical Sciences, Biosciences and Geosciences Division, the OBES, the OS, the US DOE. I would like to thank present and former members of the Nanotechnology and Advanced Spectroscopy Team at Los Alamos National Laboratory for their contributions to studies overviewed in this article.

LITERATURE CITED

1. Efros AL, Efros AL. 1982. *Sov. Phys. Sem.* 16:772–75
2. Brus LE. 1983. *J. Chem. Phys.* 79:5566–71
3. Murray CB, Norris DJ, Bawendi MG. 1993. *J. Am. Chem. Soc.* 115:8706–15
4. Peng X, Manna L, Yang WD, Wickham J, Scher E, et al. 2000. *Nature* 404:59–61
5. McDaniel H, Fuke N, Pietryga JM, Klimov VI. 2013. *J. Phys. Chem. Lett.* 4:355–61
6. Ithurria S, Tessier MD, Mahler B, Lobo RPSM, Dubertret B, Efros AL. 2011. *Nat. Mater.* 10:936–41
7. Manna L, Scher EC, Alivisatos AP. 2000. *J. Am. Chem. Soc.* 122:12700–6
8. Hines MA, Guyot-Sionnest P. 1996. *J. Phys. Chem.* 100:468–71
9. Kim S, Fisher B, Eisler H-J, Bawendi MG. 2003. *J. Am. Chem. Soc.* 125:11466–67
10. Ivanov SA, Piryatinski A, Nanda J, Tretiak S, Werder D, Klimov VI. 2007. *J. Am. Chem. Soc.* 129:11708–19
11. Shieh F, Saunders AE, Korgel BA. 2005. *J. Phys. Chem. B* 109:8538–42
12. Talapin DV, Nelson JH, Shevchenko EV, Aloni S, Sadtler B, Alivisatos AP. 2007. *Nano Lett.* 7:2951–59
13. Lee DC, Robel I, Pietryga JM, Klimov VI. 2010. *J. Am. Chem. Soc.* 132:9960–62
14. Kim H, Achermann M, Hollingsworth JA, Klimov VI. 2005. *J. Am. Chem. Soc.* 127:544–46
15. Salant A, Amitay-Sadovsky E, Banin U. 2006. *J. Am. Chem. Soc.* 128:10006–7
16. Zhang J, Tang Y, Lee K, Ouyang M. 2010. *Science* 327:1634–38
17. Colvin VL, Schlamp MC, Alivisatos AP. 1994. *Nature* 370:354–56
18. Anikeeva PO, Halpert JE, Bawendi MG, Bulović V. 2007. *Nano Lett.* 7:2196–200
19. Mueller AH, Petruska MA, Achermann M, Werder DJ, Akhadvov EA, et al. 2005. *Nano Lett.* 5:1039–44
20. Klimov VI, Mikhailovsky AA, Xu S, Malko A, Hollingsworth JA, et al. 2000. *Science* 290:314–17
21. Malko AV, Mikhailovsky AA, Petruska MA, Hollingsworth JA, Htoon H, et al. 2002. *Appl. Phys. Lett.* 81:1303–5
22. Konstantatos G, Howard I, Fischer A, Hoogland S, Clifford J, et al. 2006. *Nature* 442:180–83
23. Pal BN, Ghosh Y, Brovelli S, Laocharoensuk R, Klimov VI, et al. 2012. *Nano Lett.* 12:331–36

24. Sun B, Findikoglu AT, Sykora M, Werder DJ, Klimov VI. 2009. *Nano Lett.* 9:1235–41
25. Johnston KW, Pattantyus-Abraham AG, Clifford JP, Myrskog SH, MacNeil DD, et al. 2008. *Appl. Phys. Lett.* 92:151115
26. Luther JM, Gao J, Lloyd MT, Semonin OE, Beard MC, Nozik AJ. 2010. *Adv. Mater.* 22:3704–7
27. Nirmal M, Norris DJ, Kuno M, Bawendi MG, Efros AL, Rosen M. 1995. *Phys. Rev. Lett.* 75:3728–31
28. Efros AL, Kharchenko VA, Rosen M. 1995. *Solid State Commun.* 93:281–84
29. Klimov VI, McBranch DW. 1998. *Phys. Rev. Lett.* 80:4028–31
30. Chepic DI, Efros AL, Ekimov AI, Ivanov MG, Kharchenko VA, Kudriavtsev IA. 1990. *J. Lumin.* 47:113–27
31. Klimov VI, Mikhailovsky AA, McBranch DW, Leatherdale CA, Bawendi MG. 2000. *Science* 287:1011–13
32. Schaller RD, Klimov VI. 2004. *Phys. Rev. Lett.* 92:186601
33. Beard MC, Luther JM, Semonin OE, Nozik AJ. 2013. *Acc. Chem. Res.* 46:1252–60
34. Padilha LA, Stewart JT, Sandberg RL, Bae WK, Koh W-K, et al. 2013. *Acc. Chem. Res.* 46:1261–69
35. Klimov VI, Ivanov SA, Nanda J, Achermann M, Bezel I, et al. 2007. *Nature* 447:441–46
36. Klimov VI, Bawendi MG. 2001. *Mater. Res. Soc. Bull.* 26:998–1004
37. Hanna MC, Nozik AJ. 2006. *J. Appl. Phys.* 100:074510
38. Klimov VI. 2006. *Appl. Phys. Lett.* 89:123118
39. Landsberg PT. 1991. *Recombination in Semiconductors*. Cambridge: Cambridge Univ. Press
40. Pietryga JM, Zhuravlev KK, Whitehead M, Klimov VI, Schaller RD. 2008. *Phys. Rev. Lett.* 101:217401
41. Robel I, Gresback R, Kortshagen U, Schaller RD, Klimov VI. 2009. *Phys. Rev. Lett.* 102:177404
42. Midgett AG, Luther JM, Stewart JT, Smith DK, Padilha LA, et al. 2013. *Nano Lett.* 13:3078–85
43. Koh WK, Kaposov AY, Stewart JT, Pal BN, Robel I, et al. 2013. *Sci. Rep.* 3:2004
44. Klimov VI, McGuire JA, Schaller RD, Rupasov VI. 2008. *Phys. Rev. B* 77:195324
45. Crooker SA, Barrick T, Hollingsworth JA, Klimov VI. 2003. *Appl. Phys. Lett.* 82:2793–95
46. Kang I, Wise FW. 1997. *J. Opt. Soc. Am. B* 14:1632–46
47. Schaller RD, Petruska MA, Klimov VI. 2003. *J. Phys. Chem. B* 107:13765–68
48. McGuire JA, Sykora M, Joo J, Pietryga JM, Klimov VI. 2010. *Nano Lett.* 10:2049–57
49. Fisher B, Caruge JM, Zehnder D, Bawendi MG. 2005. *Phys. Rev. Lett.* 94:087403
50. Nair G, Bawendi MG. 2007. *Phys. Rev. B* 76:081304
51. Park YS, Malko AV, Vela J, Chen Y, Ghosh Y, et al. 2011. *Phys. Rev. Lett.* 106:187401
52. Padilha LA, Bae WK, Klimov VI, Pietryga JM, Schaller RD. 2013. *Nano Lett.* 13:925–32
53. McGuire JA, Sykora M, Robel I, Padilha LA, Joo J, et al. 2010. *ACS Nano* 4:6087–97
54. Jha PP, Guyot-Sionnest P. 2009. *ACS Nano* 3:1011–15
55. Galland C, Ghosh Y, Steinbrück A, Sykora M, Hollingsworth JA, et al. 2011. *Nature* 479:203–7
56. Connelly NG, Geiger WE. 1996. *Chem. Rev.* 96:877–910
57. Hyun B-R, Zhong Y-W, Bartnik AC, Sun L, Abruña HD, et al. 2008. *ACS Nano* 2:2206–12
58. Jasieniak J, Califano M, Watkins SE. 2011. *ACS Nano* 5:5888–902
59. Klimov VI. 2007. *Annu. Rev. Phys. Chem.* 58:635–73
60. Wehrenberg BL, Guyot-Sionnest P. 2003. *J. Am. Chem. Soc.* 125:7806–7
61. Shim M, Guyot-Sionnest P. 2000. *Nature* 407:981–83
62. Diaconescu B, Padilha LA, Nagpal P, Swartzentruber BS, Klimov VI. 2013. *Phys. Rev. Lett.* 110:127406
63. Wehrenberg BL, Wang C, Guyot-Sionnest P. 2002. *J. Phys. Chem. B* 106:10634–40
64. Chen Y, Vela J, Htoon H, Casson JL, Werder DJ, et al. 2008. *J. Am. Chem. Soc.* 130:5026–27
65. Mahler B, Spinicelli P, Buil S, Quelin X, Hermier JP, Dubertret B. 2008. *Nat. Mater.* 7:659–64
66. Bae WK, Padilha LA, Park YS, McDaniel H, Robel I, et al. 2013. *ACS Nano* 7:3411–19
67. Oron D, Kazes M, Banin U. 2007. *Phys. Rev. B* 75:035330
68. Zavelani-Rossi M, Lupo MG, Tassone F, Manna L, Lanzani G. 2010. *Nano Lett.* 10:3142–50
69. Garcia-Santamaria F, Chen YF, Vela J, Schaller RD, Hollingsworth JA, Klimov VI. 2009. *Nano Lett.* 9:3482–88
70. Garcia-Santamaria F, Brovelli S, Viswanatha R, Hollingsworth JA, Htoon H, et al. 2011. *Nano Lett.* 11:687–93

71. Cragg GE, Efros AL. 2009. *Nano Lett.* 10:313–17
72. Climente JI, Movilla JL, Planelles J. 2012. *Small* 8:754–59
73. Wang X, Ren X, Kahen K, Hahn MA, Rajeswaran M, et al. 2009. *Nature* 459:686–89
74. Osovsky R, Cheskis D, Kloper V, Sashchiuk A, Kroner M, Lifshitz E. 2009. *Phys. Rev. Lett.* 102:197401
75. Park YS, Bae WK, Padilha LA, Pietryga JM, Klimov VI. 2014. *Nano Lett.* 14: In press
76. Bae WK, Brovelli S, Klimov VI. 2013. *MRS Bull.* 38:721–30
77. Klimov VI, McBranch DW. 1997. *Phys. Rev. B* 55:13173–79
78. Kolodinski S, Werner JH, Queisser HJ. 1994. *Sol. Energy Mater. Sol. Cells* 33:275–85
79. Kolodinski S, Werner JH, Wittchen T, Queisser HJ. 1993. *Appl. Phys. Lett.* 63:2405–7
80. Werner JH, Kolodinski S, Queisser HJ. 1994. *Phys. Rev. Lett.* 72:3851–54
81. Nozik AJ. 2002. *Physica E* 14:115–20
82. Koc S. 1957. *Czechoslov. J. Phys. B* 7:91–95
83. Beard MC, Midgett AG, Hanna MC, Luther JM, Hughes BK, Nozik AJ. 2010. *Nano Lett.* 10:3019–27
84. Alig RC, Bloom S. 1975. *Phys. Rev. Lett.* 35:1522–25
85. Klein CA. 1968. *J. Appl. Phys.* 39:2029–38
86. Ellingson RJ, Beard MC, Johnson JC, Yu P, Micic OI, et al. 2005. *Nano Lett.* 5:865–71
87. Murphy JE, Beard M, Norman A, Ahrenkiel S, Johnson J, et al. 2006. *J. Am. Chem. Soc.* 128:3241–47
88. Schaller RD, Petruska MA, Klimov VI. 2005. *Appl. Phys. Lett.* 87:253102
89. Pijpers JJH, Hendry E, Milder MTW, Fanciulli R, Savolainen J, et al. 2007. *J. Phys. Chem. C* 111:4146–52
90. Schaller RD, Pietryga JM, Klimov VI. 2007. *Nano Lett.* 7:3469–76
91. Beard MC, Knutsen KP, Yu P, Luther JM, Song Q, et al. 2007. *Nano Lett.* 7:2506–12
92. Timmerman D, Izeddin I, Stallinga P, Yassievich IN, Gregorkiewicz T. 2008. *Nat. Photonics* 2:105–9
93. Semonin OE, Luther JM, Choi S, Chen HY, Gao J, et al. 2011. *Science* 334:1530–33
94. Schaller RD, Agranovich VM, Klimov VI. 2005. *Nat. Phys.* 1:189–94
95. Schaller RD, Klimov VI. 2006. *Phys. Rev. Lett.* 96:097402
96. McGuire JA, Joo J, Pietryga JM, Schaller RD, Klimov VI. 2008. *Acc. Chem. Res.* 41:1810–19
97. Nair G, Geyer SM, Chang L-Y, Bawendi MG. 2008. *Phys. Rev. B* 78:125325
98. Ben-Lulu M, Mocatta D, Bonn M, Banin U, Ruhman S. 2008. *Nano Lett.* 8:1207–11
99. Pijpers JJH, Hendry E, Milder MTW, Fanciulli R, Savolainen J, et al. 2008. *J. Phys. Chem. C* 112:4783–84
100. Trinh MT, Houtepen AJ, Schins JM, Hanrath T, Piris J, et al. 2008. *Nano Lett.* 8:1713–18
101. Midgett AG, Hillhouse HW, Huges BK, Nozik AJ, Beard MC. 2010. *J. Phys. Chem. C* 114:17486–500
102. Padilha LA, Robel I, Lee DC, Nagpal P, Pietryga JM, Klimov VI. 2011. *ACS Nano* 5:5045–55
103. Pijpers JJH, Ulbricht R, Tielrooij KJ, Osherov A, Golan Y, et al. 2009. *Nat. Phys.* 5:811–14
104. Shockley W, Queisser HJ. 1961. *J. Appl. Phys.* 32:510–19
105. Sandberg RL, Padilha LA, Qazilbash MM, Bae WK, Schaller RD, et al. 2012. *ACS Nano* 6:9532–40
106. Padilha LA, Stewart JT, Sandberg RL, Bae WK, Koh W-K, et al. 2013. *Nano Lett.* 13:1092–99
107. Timmerman D, Valenta J, Dohnalova K, de Boer WDAM, Gregorkiewicz T. 2011. *Nat. Nanotechnol.* 6:710–13
108. Trinh MT, Limpens R, de Boer WDAM, Schins JM, Siebbeles LDA, Gregorkiewicz T. 2012. *Nat. Photonics* 6:316–21
109. Allan G, Delerue C, Pijpers JJ, Bonn M. 2010. *Phys. Rev. B* 81:125306
110. Califano M. 2011. *ACS Nano* 5:3614–21
111. Califano M, Zunger A, Franceschetti A. 2004. *Nano Lett.* 4:525–31
112. Rabani E, Baer R. 2010. *Chem. Phys. Lett.* 496:227–35
113. Baer R, Rabani E. 2012. *Nano Lett.* 12:2123–28
114. Allan G, Delerue C. 2006. *Phys. Rev. B* 73:205423
115. Shabaev A, Efros AL, Nozik AJ. 2006. *Nano Lett.* 6:2856–63
116. Witzel WM, Shabaev A, Hellberg CS, Jacobs VL, Efros AL. 2010. *Phys. Rev. Lett.* 105:137401
117. Prezhdov OV. 2008. *Chem. Phys. Lett.* 460:1–9
118. Hyeon-Deuk K, Prezhdov OV. 2012. *J. Phys. Condens. Matter.* 24:363201

119. Hyeon-Deuk K, Prezhdov OV. 2012. *ACS Nano* 6:1239–50
120. Rupasov VI, Klimov VI. 2007. *Phys. Rev. B* 76:125321
121. Govoni M, Marri I, Ossicini S. 2012. *Nat. Photonics* 6:672–79
122. Stewart JT, Padilha LA, Bae WK, Koh W-K, Pietryga JM, Klimov VI. 2013. *J. Phys. Chem. Lett.* 4:2061–68
123. Charache GW, Baldasaro PF, Danielson LR, DePoy DM, Freeman MJ, et al. 1999. *J. Appl. Phys.* 85:2247–52
124. Schaller RD, Pietryga JM, Goupalov SV, Petruska MA, Ivanov SA, Klimov VI. 2005. *Phys. Rev. Lett.* 95:196401
125. Klimov VI, McBranch DW, Leatherdale CA, Bawendi MG. 1999. *Phys. Rev. B* 60:13740–49
126. Yang J, Hyun BR, Basile AJ, Wise FW. 2012. *ACS Nano* 6:8120–27
127. Wang F, Wu Y, Hybertsen MS, Heinz TF. 2006. *Phys. Rev. B* 73:245424
128. Bartnik AC, Efros AL, Koh WK, Murray CB, Wise FW. 2010. *Phys. Rev. B* 82:195313
129. Achermann M, Bartko AP, Hollingsworth JA, Klimov VI. 2006. *Nat. Phys.* 2:557–61
130. Htoon H, Hollingsworth JA, Dickerson R, Klimov VI. 2003. *Phys. Rev. Lett.* 91:227401
131. Stewart JT, Padilha LA, Qazilbash MM, Pietryga JM, Midgett AG, et al. 2012. *Nano Lett.* 12:622–28